REACTION PATHWAY FOR THE AEROBIC OXIDATION OF PHOSPHINES CATALYZED BY OXOMOLYBDENUM SALEN COMPLEXES

Theo A. Rusmore, Chance Lander and Kenneth M. Nicholas*
Department of Chemistry and Biochemistry, 101 Stephenson Pkwy.
University of Oklahoma, Norman, OK 73019

Abstract. Catalysis of *O*-atom transfer (OAT) reactions is a characteristic of both natural (enzymatic) and synthetic molybdenum-oxo and -peroxo complexes. These reactions can employ a variety of terminal oxidants, e.g. DMSO, *N*-oxides, and peroxides, etc., but rarely molecular oxygen. Here we demonstrate the ability of a set of Schiff-base-MoO_2 complexes (cy-salen)MoO_2 (cy-salen= *N,N'*-cyclohexyl-1,2-bis-salicylimine) to catalyze the aerobic oxidation of PPh_3. We also report the results of a DFT computational investigation of the catalytic pathway, including the identification of energetically accessible intermediates and transition states, for the aerobic oxidation of PMe_3. Starting from the dioxo species, (cy-salen)Mo(VI)O_2 (**1**), key reaction steps include: 1) associative addition of PMe_3 to an oxo-O to give LMo(IV)(O)($OPMe_3$) (**2**); 2) $OPMe_3$ dissociation from **2** to produce mono-oxo complex (cy-salen)Mo(IV)O (**3**); 3) stepwise O_2 association with **3** via superoxo species (cy-salen)Mo(V)(O)(η^1-O_2) (**4**) to form the oxo-peroxo intermediate (cy-salen)Mo(VI)(O)(η^2-O_2) (**5**); 4) the *O*-transfer reaction of PMe_3 with oxo-peroxo species **5** at the oxo-group, rather than the peroxo unit leading, after $OPMe_3$ dissociation, to a monoperoxo species, (cy-salen)Mo(IV)(η^2-O_2) (**7**); and 5) regeneration of the dioxo complex (cy-salen)Mo(VI)O_2 (**1**) from the monoperoxo triplet ^{3}**7** or singlet ^{1}**7** by a concerted, asynchronous electronic isomerization. An alternative pathway for recycling of the oxo-peroxo species **5** to the dioxo-Mo **1** via a bimetallic peroxo complex LMo(O)-O-O-Mo(O)L **8** is determined to be energetically viable but is unlikely to be competitive with the primary pathway for aerobic phosphine oxidation catalyzed by **1**.

Keywords

aerobic oxidation, molybdenum-oxo-peroxo complex, oxo/peroxo group reactivity, phosphine oxidation, metal-peroxo to -dioxo isomerization

A. Introduction

Oxygen-atom transfer (OAT) reactions (*eq. 1*), involving the gain or loss of an oxygen atom from a substrate, can be mediated by oxo-transition metal complexes, be they synthetic or natural (i.e. enzymes) (*eq. 2*). In the biological domain the most prevalent metal-oxo species involved in OAT are of iron, as in heme- and non-heme enzymes, and of molybdenum. The latter oxo-metal center appears in more than 50 redox enzymes, making up the xanthine oxidase, sulfite oxidase, and DMSO reductase families.[1,2]

$$X + AO \rightarrow XO + A \qquad \textit{eq. 1}$$

$$M^nO_xL + X \rightleftharpoons M^{n-2}O_{x-1}L + XO \qquad \textit{eq. 2}$$

The Mo-oxotransferases and synthetic oxo-molybdenum complexes can employ a variety of oxygen atom donor/acceptor substrates, including as donors DMSO, nitrate, and amine oxides and as acceptors sulfite, carbon monoxide, formate, xanthine, and phosphines.[1,3–6] Structure/reactivity, thermodynamic and mechanistic studies of synthetic oxo-molybdenum species have provided some insights into the energetics and mechanism of *O*-transfer to/from oxo-metal species.[7,8] The OAT oxidation of phosphines, in particular, has served as a convenient benchmark reaction for oxo-metal reactivity and a useful system for mechanistic study.[9,10] With phosphine substrates the OAT reaction is thought to proceed in a stepwise manner, involving nucleophilic attack by the phosphine on the electrophilic oxo oxygen of the oxo-Mo(VI) species, giving an intermediate Mo(IV) phosphine oxide complex, which undergoes dissociation to the reduced LMo(IV) product and OPR_3 (Figure 1).

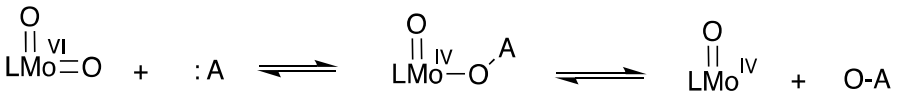

Figure 1. General oxygen atom transfer reaction with molybdenum-oxo species

Metal-dioxygen complexes, LM(O-O), isomeric with dioxo-metal species, also feature prominently in catalytic oxidation reactions. Dioxygen coordination, is typically manifested in the formation of metal-superoxo (η^1-, **C**) or peroxo (η^2-; **B**, **D**-**F**) complexes (Figure 2), and the reactivity of these species has been extensively studied for many transition metals.[11–19] The oxidative ability of dioxygen (peroxo) complexes, has sparked interest in using dioxygen to form the molybdenum-peroxo species directly in an atom-economical fashion.[20] Prior studies have documented the ability of (porphyrin)Mo(IV)-oxo complexes to reversibly bind O_2.[21–23] The resulting oxo-peroxo complexes (POR)Mo(VI)(O)(η^2-O_2) can release O_2 photochemically and have been considered for oxygen transport and storage systems.[22,24,25] Additionally, synthetic molybdenum peroxo compounds have been used as reagents and catalysts in the production of epoxides from alkenes, the oxidations of alcohols,[26] and sulfoxidation reactions,[27] with either hydrogen peroxide or *tert*-butyl hydrogen peroxide as terminal oxidants.[28–30]

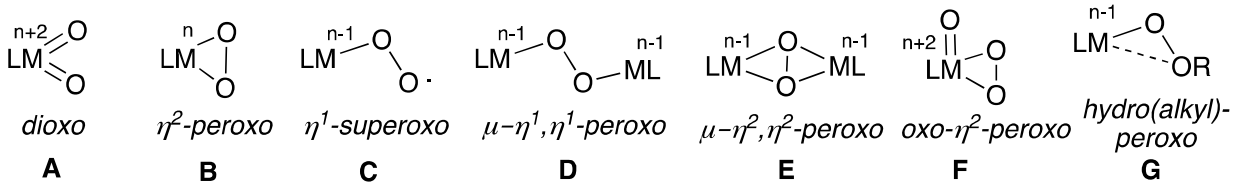

Figure 2. Types of coordinated oxygen and related species

In catalytic reactions involving oxo- or peroxo species, these reactive intermediates may potentially interconvert via bridged peroxo compounds, e.g. **D**,**E**, via a Mars-van Krevelen-type mechanism (Figure 3).[31–34] This potential equilibrium can obscure the identity of the actual active oxidizing species.

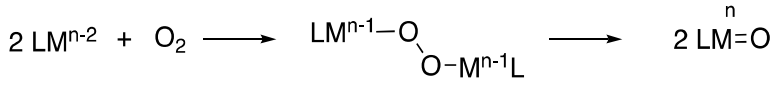

Figure 3. Bimetallic Mars-Van Krevelen mechanism for transition metal splitting of dioxygen to dioxo-M species

Much of the prior work on molybdenum-peroxo (dioxygen) catalysis has focused on oxo-*bis*-peroxomolybdenum(VI) species, $LMo(O)(\eta^2\text{-}O_2)_2$, employing peroxidic reagents as stoichiometric oxidants. Epoxidations via these species are typically considered to proceed via direct transfer of a peroxo oxygen to the olefin double bond,[35] which is supported by a limited number of computational and experimental studies, including *O*-labeling experiments.[35–40] O-transfer reactivity involving presumed coordination of dioxygen to a molybdenum center was posited by Arzoumanian, et al.[41], who found that $MoO(\eta^2\text{-}O_2)(CN)_x^{2-}$ reacts with 3 equivalents of PR_3, indicating reaction of all three Mo-bound oxygen atoms.[18,42–47] Subsequently, the Mösch-Zanetti group[20,42,48,49] reported the formation of LMo(oxo)(η^2-peroxo) complexes from the reaction of (*N,O*-iminophenolate)$_2$MoZ (Z=NPh, O) with dioxygen.[48] The OAT reactivity of this oxoperoxo complex with triphenylphosphine[42,49] was investigated with O_2 as stoichiometric oxidant; it was presumed that this process involved *O*-transfer from the peroxo unit.

Further investigation, both experimentally and computationally, of O_2-based catalytic oxidations by oxo- and oxo-peroxo-forming molybdenum complexes would aid in establishing and understanding the relative reactivity of these metal-centered functional groups and their potential interconversion. To our knowledge, no computational study has been carried out on the OAT reactivity of metal oxo-peroxo complexes with substrates other than olefins, e.g. with phosphines. Experimentally, limited catalyst structure/reactivity and mechanistic information is available for such reactions.[21,40,42,44,45,48–52] In the present study we demonstrate the ability of a set of (cy-salen)MoO_2 complexes to catalyze the aerobic oxidation of phosphines and we investigate computationally the catalytic pathway, providing evidence for here-to-fore unexpected selective reactivity of the oxo- vs. the peroxo- units present in key transformations, as well as evidence for a novel metal-peroxo to metal-dioxo redox isomerization.

B. Results and Discussion

B-1. *Oxygen as the terminal oxidant for phosphines catalyzed by (cy-salen)MoO_2 (**1**)*

We recently reported on the ability of chiral Schiff-base complexes (cy-salen)MoO_2 (**1a-1e**, Figure 4) to catalyze the oxidative kinetic resolution of *P*-chiral tertiary phosphines with pyridine *N*-oxide as the terminal oxidant.[4] Incidentally, we found that, if conducted open to the air, these reactions would proceed beyond the conversion of phosphine expected based on the loading of pyridine *N*-oxide. For example, when a chloroform solution containing 1.0 mmol of PPh_3, 0.40 mmol of pyridine *N*-oxide and 0.01 mmol of (2-Br-4-NO_2-cy-salen)MoO_2 (**1a**) was heated at 60 °C in air, a 70% yield of $OPPh_3$ (0.70 mmol) was produced (Figure 5). This observation suggested to us that oxygen in the air could be acting as a reagent for the reaction.

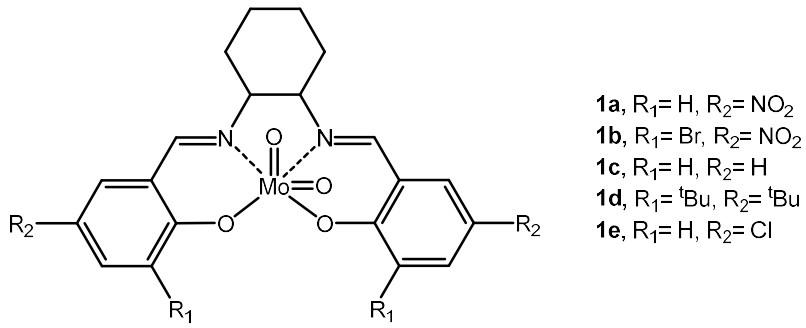

Figure 4. (Cy-salen)MoO_2 complexes **1a-e** used in this study

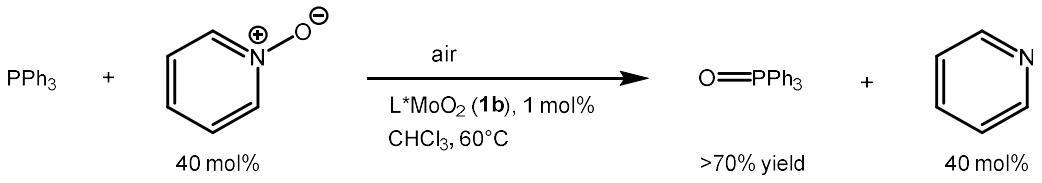

Figure 5. Observed over-conversion of Ph_3P by pyridine *N*-oxide in air catalyzed by **1b**

To explore the broader use of dioxygen as a stoichiometric oxidant, the reaction of triphenyl phosphine was conducted under air in the absence of an organic oxygen donor, with complex **1b** (Figure 5). The overall conversion rate of the reaction at 60°C in 1,1,2,2-tetrachloroethane was roughly the same as observed for the reactions involving pyridine *N*-oxide

as the oxygen atom donor.[4] ^{31}P NMR monitoring of this reaction showed the formation of two phosphorus-containing products, which are assigned as triphenylphosphine oxide (δ=29.7 ppm) and the triphenylphosphine oxide ternary complex, (cy-salen)MoO(OPPh$_3$) (δ=20.3 ppm). (see SI).[5] Catalytic phosphine oxidation under air was further studied by ^{31}P NMR monitoring at 50°C, revealing that complex **1b** provides a TON in excess of 950 (70 h), with an average TOF of 1/10 min^{-1}. Control reactions with PPh$_3$ in the absence of catalyst **1a** under the same conditions showed a small degree of autooxidation to OPPh$_3$, 3-5 % vs. 14-31% with catalyst, depending on the atmosphere over the reaction, air or pure O_2 (Figure 6). It was also found that an increase of dioxygen concentration in solution increases the rate of reaction, approximately threefold when conducting the reaction under pure dioxygen (pO_2 = 1.0 atm).

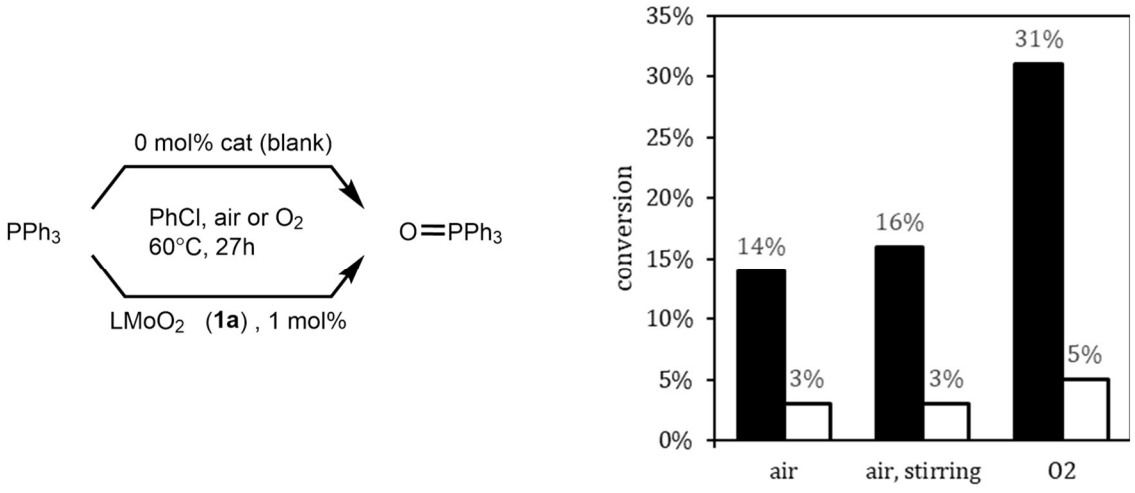

Figure 6. (a) (left) Uncatalyzed and catalyzed oxidation of PPh$_3$; (b) (right) comparative conversions for uncatalyzed (empty bar) and catalyzed (solid bar) aerobic oxidation of PPh$_3$ by **1a** (60 °C, PhCl solvent, 27h)

In order to assess the catalyst structure/activity relationship for aerobic PPh$_3$ oxidation, reactions were carried out with a series of *para*-substituted cy-salen complexes (*p*-nitro **1a**, *p*-H **1c**, 3,5-*tert*-butyl **1d**, and *p*-chloro **1e**). The aerobic oxidation of triphenylphosphine was promoted by all of these compounds at 1 mol % loading. Examination of the initial reaction rates for **1a** and **1c-1e** (Figure 7) shows that there is a linear Hammett relationship[53] between the rate of oxidation and the σ-value of ligand substituent (Figure 8). *Para*-substitution of the

salicylimine ring with electron-withdrawing groups accelerates the reaction, while an electron donating group slows it, with a rho (ρ) value of 0.54. In comparison with the results of Whiteoak et al. for the analogous salan-type dioxomolybdenum series for the oxidation of PPh_3 by DMSO,[10] the *p*-substituents had a lesser effect (smaller rho value) on the reaction rate catalyzed by **1**. The Hammett correlation for the present (cy-salen)MoO_2-catalyzed reaction is consistent with, but does not prove, that the turnover-limiting step is one in which the nucleophilic phosphine attacks an electrophilic molybdenum(VI) center.

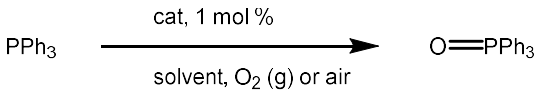

catalyst	mol %	solvent	T	atm	t	conversion
1c	1	PhCl	50 °C	O_2	13h	4%
1d	1	PhCl	50 °C	O_2	13h	4%
1e	1	PhCl	50 °C	O_2	13h	6%
1a	1	PhCl	50 °C	O_2	13h	10%

Figure 7. Aerobic oxidation of PPh_3 by (cy-salen)dioxomolybdenum complexes **1a**, **1c-1e**

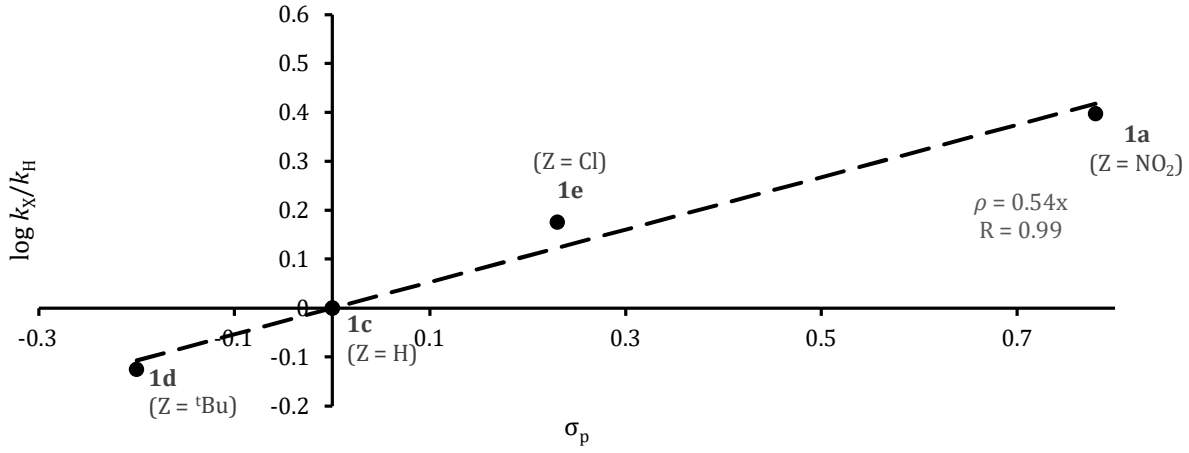

Figure 8. Relationship between relative rate constants, log k_X/k_H, and Hammett parameter σ_p for the reaction of dioxygen and PPh_3 catalyzed by (*p*-Z-cy-salen)MoO_2 (**1**).

B-2. Modeling the aerobic (Cy-salen)MoO_2-mediated OAT to PMe_3

Based on the preliminary experimental study and prior reports of OAT from oxo-molybdenum compounds to phosphines (typically PPh_3), we hypothesized that the catalytic cycle would initially involve OAT from the dioxo species **A** to PMe_3, association of dioxygen with the monooxo Mo(IV) complex LMo(O) (**H**) to form an oxo-peroxo species, $LMo^{VI}(O)(O_2)$ (**F**), and a second OAT from the oxo-peroxo intermediate **F** to the phosphine to regenerate the dioxo catalyst **A** (Figure 9).

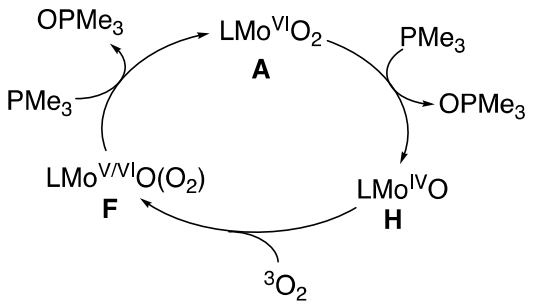

Figure 9. Putative catalytic process for aerobic oxidation of PMe_3 by (cy-salen)MoO_2.

We selected trimethyl phosphine (PMe_3) as the model phosphine for the computational studies, as is often done, for computational economy. It is acknowledged to be more basic and less sterically hindered relative to the experimental PPh_3, which could quantitatively affect the energetic profile for various reaction pathways. To gain some perspective on the magnitude of the difference between PMe_3 and PPh_3, we include subsequently a comparison of calculated activation barriers for the *O*-transfer reaction of (cy-salen)MoO_2 (**1a**) with both PPh_3 vs. PMe_3. To determine the most likely pathway of this reaction, potential stationary state species were optimized using the B3LYP hybrid functional in the gas phase. Transition states were located using relaxed mod-redundant scans along the forming/breaking bond and optimized to a Berny transition state using the B3LYP functional.[54,55] All energies for solvated species (SMD 1,1,2,2-tetrachloroethane) were obtained with a single point calculation with the M06 functional.[56] The hybrid B3LYP and M06 DFT functionals have been the most commonly employed to model the structures, reactivity and energetics of a diversity of molybdenum complexes.[57]

B-2a. *Oxidation of PMe_3 by (Cy-salen)MoO_2 (**1a**)*

The B3LYP-optimized geometry of the starting dioxomolybdenum complex **1a** is shown in Figure 10. The C_1 *cis*-dioxo species has inequivalent oxo groups, one *trans* to one of the imine *N*-ligand atoms (equatorial), and one *trans* to the phenolate moiety (axial) and a distinctly unsymmetrical octahedral geometry. This unsymmetrical structure is supported by NMR studies and calculated to be 8-10 kcal/mol more stable than a potential C_2-isomer.[4] Based on our computational study of the kinetic resolution of chiral tertiary phosphines by pyridine *N*-oxide catalyzed by (cy-salen)MoO_2,[4] only the lower energy axial approach of phosphine to the dioxo complex **1a** was considered. The transition state for axial attack of **1a** by PMe_3 $\mathbf{TS_{1a\text{-}2}}$ was located (Figure 11) and optimized to an activation energy that is 20.1 kcal/mol uphill from the reactants. A frontier orbital analysis of **1a** shows that orbitals with contribution on the equatorial oxygen are either significantly stabilized (oxo lone pair) or higher in energy (Mo-O π^* orbitals), whereas the frontier unoccupied orbitals, e.g. LUMO itself, has a larger contribution from the axial O (Figure 10b). As the phosphine approaches, there is a reduction in the bond order of the axial Mo-oxo moiety, with the Mo-O bond length increasing from 1.72 Å to 1.85 Å. The HOMO of the TS has an orbital contribution with P-O bonding and Mo-O antibonding character in the forming O-P σ-bond (Figure 11b), and a P-O distance of 2.06 Å, indicative of a bond order lower than that in the product ternary complex **2** and the free phosphine oxide. Calculations of the oxygen atom transfer transition state and activation energy for **1a** to PPh_3, by comparison, gave a slightly higher $\Delta G^{\ddagger}$ of 22.5 kcal/mol, consistent with the lower nucleophilicity and greater steric bulk of the triaryl phosphine substrate.

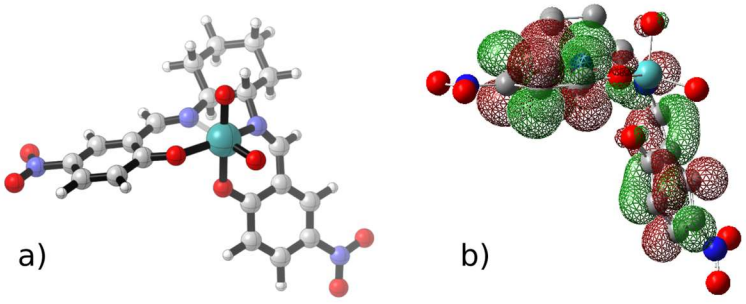

Figure 10. (a) B3LYP-optimized structure of dioxo-Mo complex **1a**; Mo=O(ax) 1.73 Å, Mo=O(eq) 1.72 Å, Mo-O 1.98 and 2.18 Å and Mo-N 2.38 and 2.16 Å; (b) LUMO for **1a**, H-atoms omitted for clarity.

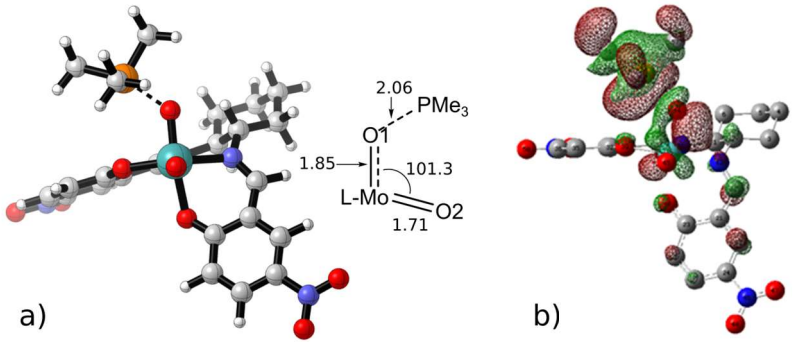

Figure 11. (a) (left) **TS$_{1\text{-}2}$** for axial oxido attack by PMe_3 on **1a**; selected bond lengths (Å) and angles (°) are shown in the inset. (b) (right) HOMO for TS of PMe_3-attack on the axial oxido-*O*; hydrogen atoms are omitted for clarity.

The energetic driving force of the oxygen atom transfer reaction is the formation of the ternary complex **2**, 27.6 kcal/mol downhill energetically from the starting materials (Figure 12). The P-O bond order has increased to nearly a full double bond (1.53 Å) of the free phosphine oxide (1.50 Å), while the Mo-O bond order has reduced to a weak single bond (2.35 Å). The molybdenum complex has begun reorganizing toward the square pyramidal coordination of the monooxo complex **3**, allowing the O-Mo-O angle to decrease to 83.9°.

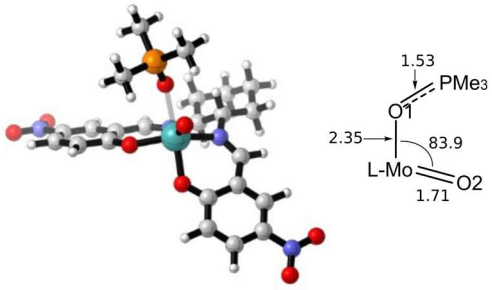

Figure 12. Ternary phosphine oxide complex **2**; selected bond lengths (Å) and angles (°) are shown in the inset.

The next step in the *O*-transfer process is $OPMe_3$ dissociation. As the phosphine oxide dissociates from the metal center (activation energy 6.7 kcal/mol), the molecule begins reorganizing toward square pyramidal (cy-salen)MoO (**3**) (Figure 13) via transition state **TS$_{2\text{-}3}$**

(Figure 13) with the Mo-O bond nearly cleaved at 2.97 Å. The P-O bond order continues to increase as the back-bonding contribution from the molybdenum center decreases, leading to a P-O bond slightly lengthened compared to the free phosphine oxide (1.50 Å).

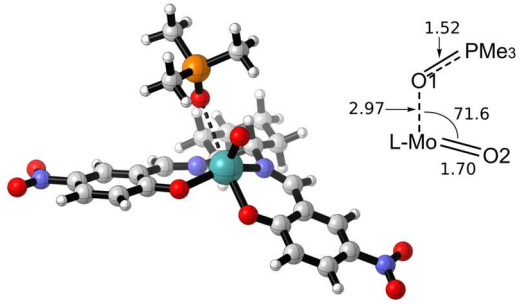

Figure 13. Transition state for dissociation of $OPMe_3$ from ternary complex **2**, $\mathbf{TS_{2\text{-}3}}$; selected bond lengths (Å) and angles (°) are shown in the inset.

Following dissociation of the phosphine oxide, reorganization of the oxo-Mo salen complex has completed to form the monooxo-Mo compound **3**. For the singlet species (Figure 14) the Mo-O bond order for the remaining oxo has increased slightly, with the bond length contracting to 1.69 Å (from 1.72 Å in the dioxo species). The singlet Mo(IV) monooxo complex and product phosphine oxide are stabilized by 27.3 kcal/mol relative to the reactant dioxomolybdenum **1a** and trimethylphosphine and are nearly thermoneutral (+0.3 kcal/mol) with respect to the ternary phosphine oxide complex **2**. The triplet state of the d^2-Mo(IV) monooxo complex ^{3}**3** was also optimized (see SI), but it was found to be 11.3 kcal/mol higher in energy than the singlet and hence was not considered to play a significant role in the catalytic oxidation pathway.

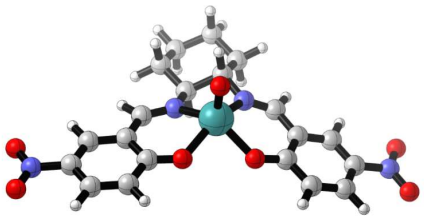

Figure 14. Monooxo molybdenum(IV) complex [13]

The reaction energy profile for oxidation of trimethyl phosphine by $LMoO_2$ **1a** (Figure 15) is very similar to that determined for the oxidation of PMePh^{t}Bu.[4] The activation energy for the oxygen atom transfer step with PMe_3 is slightly lower, 20.1 kcal/mol, vs. PMePh^{t}Bu +22.9 kcal/mol, likely due to the increased nucleophilicity and decreased steric interactions of the smaller phosphine. The ternary OPR_3 complex, dissociative transition state, and products all have relative energies nearly identical to the PMePh^{t}Bu derivative with the (cy-salen)MoO_2,[4] when adjusted for the difference in activation energy for the OAT step. The formation of the strong P-O bond of the product is the driving force of the reaction.

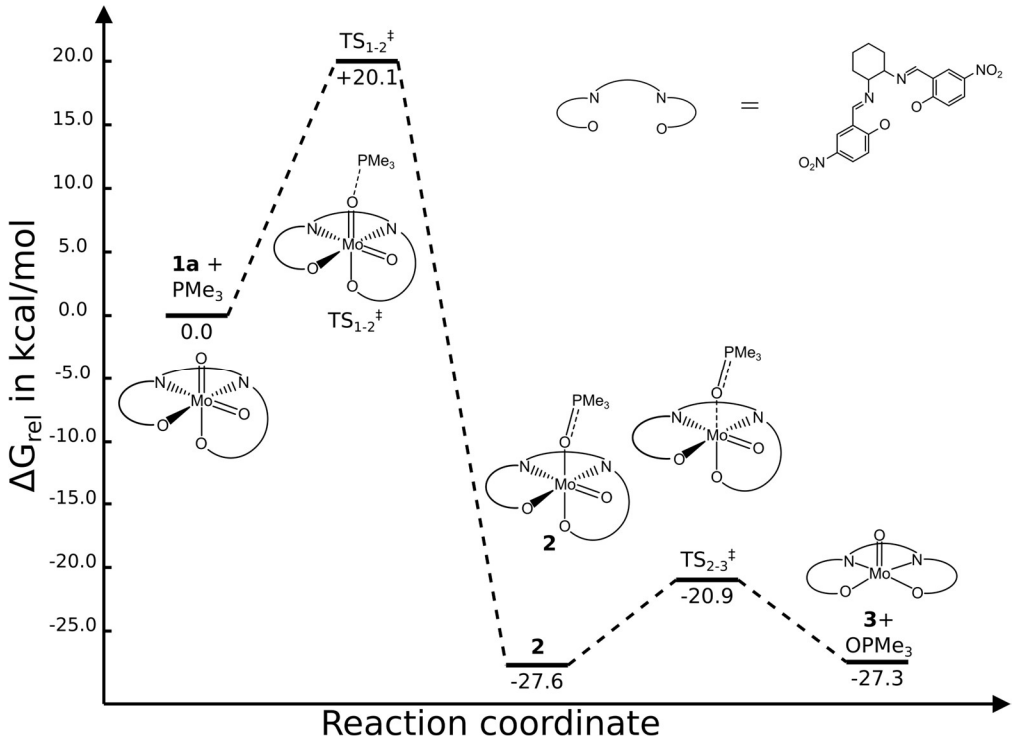

Figure 15. Reaction profile for OAT from (cy-salen)MoO_2 (**1a**) to trimethylphosphine

B-2b. *Coordination of dioxygen by (cy-salen)Mo(IV)O (**3**)*

The coordination of dioxygen to molybdenum centers has been known for some time,[20,41,42,58] but the mechanism of dioxygen association and the OAT reactivity of the resulting oxo-peroxo molybdenum(VI) species have not been explored appreciably by QM computation. Based on the experimental results presented in the prior section and the Mo-promoted aerobic phosphine oxidations reported by Arzoumanian[41,58] and Mösch-Zanetti,[20,42,48,49] the oxygenation of the (cy-salen)Mo(IV)-oxo complex **3** to the molybdenum(VI) oxo-peroxo species **5** was first considered to occur at a single-metal center, analogous to the coordination of dioxygen to ruthenium examined by Yu, et al.[59] A bimetallic coordination process, as in the Mars-Van Krevelen mechanism,[41,58,60] is evaluated subsequently.

Oxygenation of the singlet monooxo-Mo(IV) complex **3** would begin with its coordination to triplet dioxygen $^3O_2$ (Figure 16). A transition state structure for this association was located by scanning the distance between the molybdenum center and the O-O bond centroid, starting from the η^1-superoxo complex **4** (Figure 17) (*vide infra*). Two possible coordinative approaches were evaluated, with the equatorial one (Figure 17) being modestly preferred ($\Delta G^{\ddagger}$ = 5.8 kcal/mol) over the axial ($\Delta G^{\ddagger}$ = 7.1 kcal/mol). In **TS$_{3\text{-}4eq}$** as the dioxygen molecule approaches the metal center the molecule is reorganizing toward an octahedral geometry, accompanied by a small increase of the O-O bond length, from 1.21 Å to 1.23 Å. The dioxygen moiety still has diradical character in the transition state, with spin density largely concentrated in the Mo-O_2 unit.

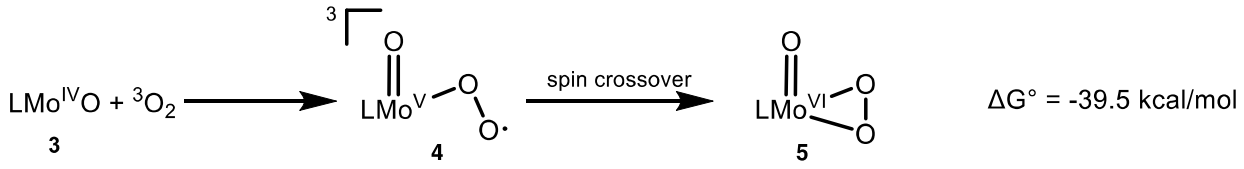

Figure 16. Coordination of dioxygen to LMo(IV)O (**3**) forming superoxo (**4**) and peroxo (**5**) complexes

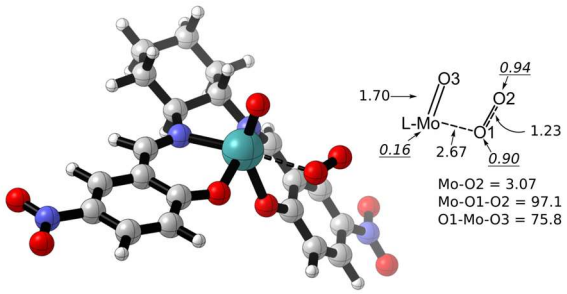

Figure 17. Transition state structure for equatorial ligation of dioxygen **TS$_{3\text{-}4\ eq}$**; selected bond lengths (Å) and angles (°) are shown in the inset, atomic spin densities are underlined/ italicized.

Following the associative transition state, a stable structure for the triplet oxo-superoxo species **4** was located for both coordination isomers with negligible difference in energies, ΔG_{ax} = -4.5 kcal/mol, ΔG_{eq} = -4.6 kcal/mol (Figure 18). The key contribution to η^1-bonding is found in the HOMO-2 orbital, involving a bonding interaction from overlap between a molybdenum d-orbital and the dioxygen π^* orbital (Figure 19b). The spin densities for the superoxo complex **4** indicate that coordination of dioxygen has led to a partially oxidized metal species (formally Mo^V), with the majority of spin density on Mo and O2 and less on O1 (Figure 19a).

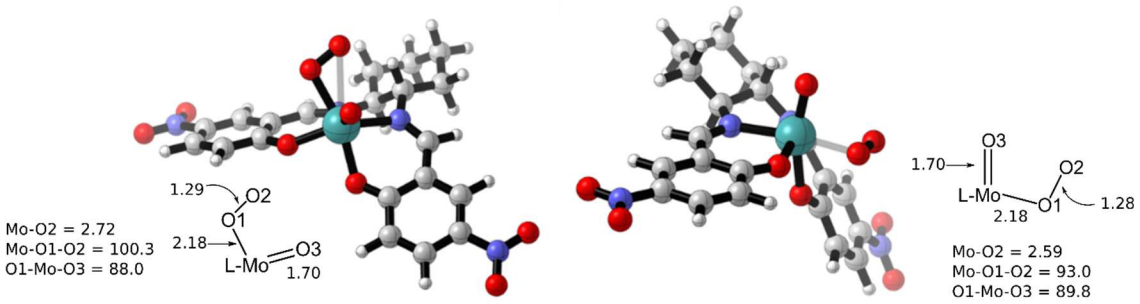

Figure 18. Optimized structures for superoxo complexes ^{3}**4$_{ax}$** (left) and ^{3}**4$_{eq}$** (right); selected bond lengths (Å) and angles (°) are shown in the inset.

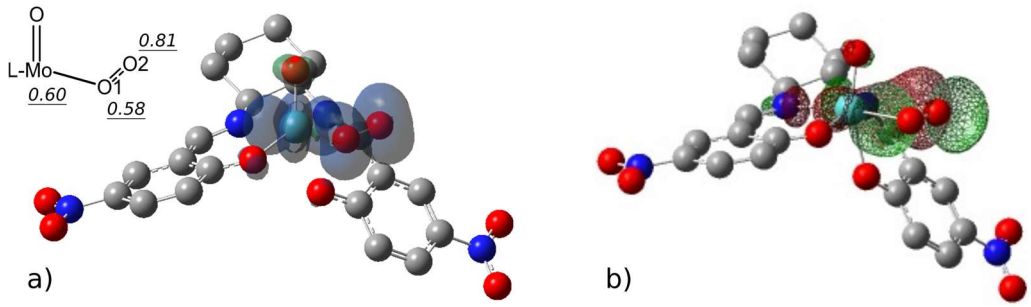

Figure 19. (a) Spin density map for $^{3}\mathbf{4}_{eq}$ (left); italicized/underlined numbers are spin densities. (b) HOMO-2 of $^{3}\mathbf{4}_{eq}$ showing Mo d/O-O π* interaction (right); H-atoms are omitted for clarity.

To form the more stable singlet oxo-peroxo intermediate **5** (*vide infra*) from the triplet superoxo species **4**, the next step would involve a spin-crossover,[61] in this case from the triplet to the singlet. The minimum energy crossing point (MECP), the lowest energy point along the intersection of the two involved potential energy surfaces, can be located using gradient-based optimizations, for which we employed the sobMECP algorithm.[62] The MECPs were located from either reactant/product pairs or points from the internal reaction coordinate calculations. The calculated structures for the triplet-to-singlet MECP in the dioxygen coordination process display some notable differences between the axial and equatorial coordination isomers, particularly in the coordination modes of the dioxygen moieties (Figure 20). The equatorial coordination isomer $\mathbf{4}_{eq}$ shows more symmetrical η^2-like binding (Mo-O1 = 2.11 Å, Mo-O2 = 2.35 Å, Mo-O1-O2 = 83.3°) and a decrease in O-O bond order, with the O-O bond length increasing to 1.31 Å. Meanwhile, the Mo-O distances for the axial coordination isomer are more different, making the binding coordination mode of the dioxygen unit more end-bound in character (Mo-O1 = 2.02 Å, Mo-O2 = 3.01 Å, Mo-O1-O2 = 131°). The activation barrier to this crossover is also quite different between the two isomers, with $\Delta G^{\ddagger}$ for the equatorial peroxo only 0.1 kcal/mol and $\Delta G^{\ddagger}$ for the axial +6.2 kcal/mol.

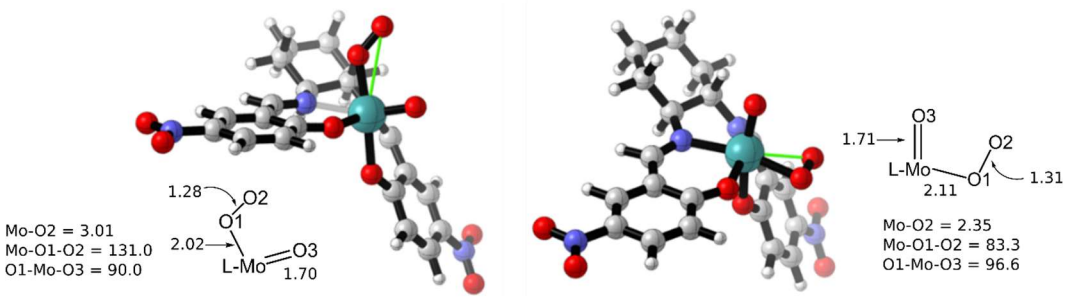

Figure 20. Calculated structures for oxo-peroxo triplet to singlet **MECP$_{4\text{-}5}$** (axial, left; equatorial, right); selected bond lengths (Å) and angles (°) are shown in the inset.

The singlet oxo-peroxo species **5** is stabilized relative to **MECP$_{4\text{-}5}$** by 24.1 kcal/mol for the axial species, 19.2 kcal/mol for the equatorial, and 15-20 kcal relative to triplet oxo-peroxo. The axial isomer **5$_{eq}$** is 4 kcal more stable than the equatorial **5$_{ax}$** (Figure 21). Each shows a symmetrically bound η^2-dioxygen moiety, and the side-on binding mode leads to significant decrease in the O-O bond order. Interestingly, the O-Mo-(O_2) bond angles are nearly equivalent to the O-Mo-O bond angle in the dioxo species. The calculated bond metrics of **5$_{eq}$** compare well with the X-ray structure of (phenoxy-imino)$_2$Mo(O)(η^2-O_2):[42] Mo=O 1.69 Å, Mo-O 1.94 Å, 1.95 Å; O-O 1.43 Å; vs. for **5$_{eq}$** Mo=O 1.71 Å, Mo-O 1.96, 1.96 Å, O-O 1.41 Å.

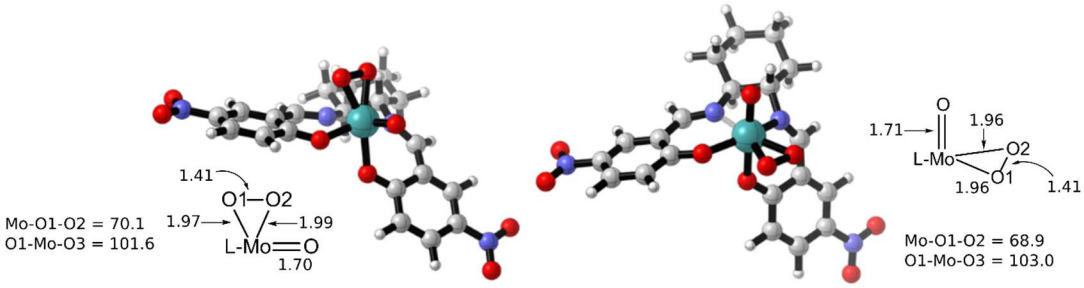

Figure 21. Singlet oxo-peroxo Mo(VI) complexes **5$_{ax}$** and **5$_{eq}$;** selected bond lengths (Å) and angles (°) are shown in the inset.

The reaction profile for coordination of dioxygen to the oxo-molybdenum(IV) complex **3** (Figure 22) is shown to be overall exergonic, with the formation of the singlet, η^2-peroxo species

5 serving as the driving force for the oxygen coordination steps. The located transition state for initial coordination of triplet dioxygen, **TS$_{3\text{-}4}$**, has a moderate energetic barrier, as does the spin-crossover step for the axial complex, **MECP$_{4\text{-}5\ ax}$**. The triplet superoxo complex, **4**, is moderately destabilized relative to the starting materials, but the modest barrier for spin-crossover from the axial complex (+8.7 kcal/mol) and near barrier-less crossover from the equatorial complex (+0.1 kcal/mol) indicates a facile conversion to the very stable singlet oxo-peroxo molybdenum (VI) complex **5**. Throughout the conversion of mono-oxo **3** to oxo-peroxo **5** the equatorial association of dioxygen remains favored.

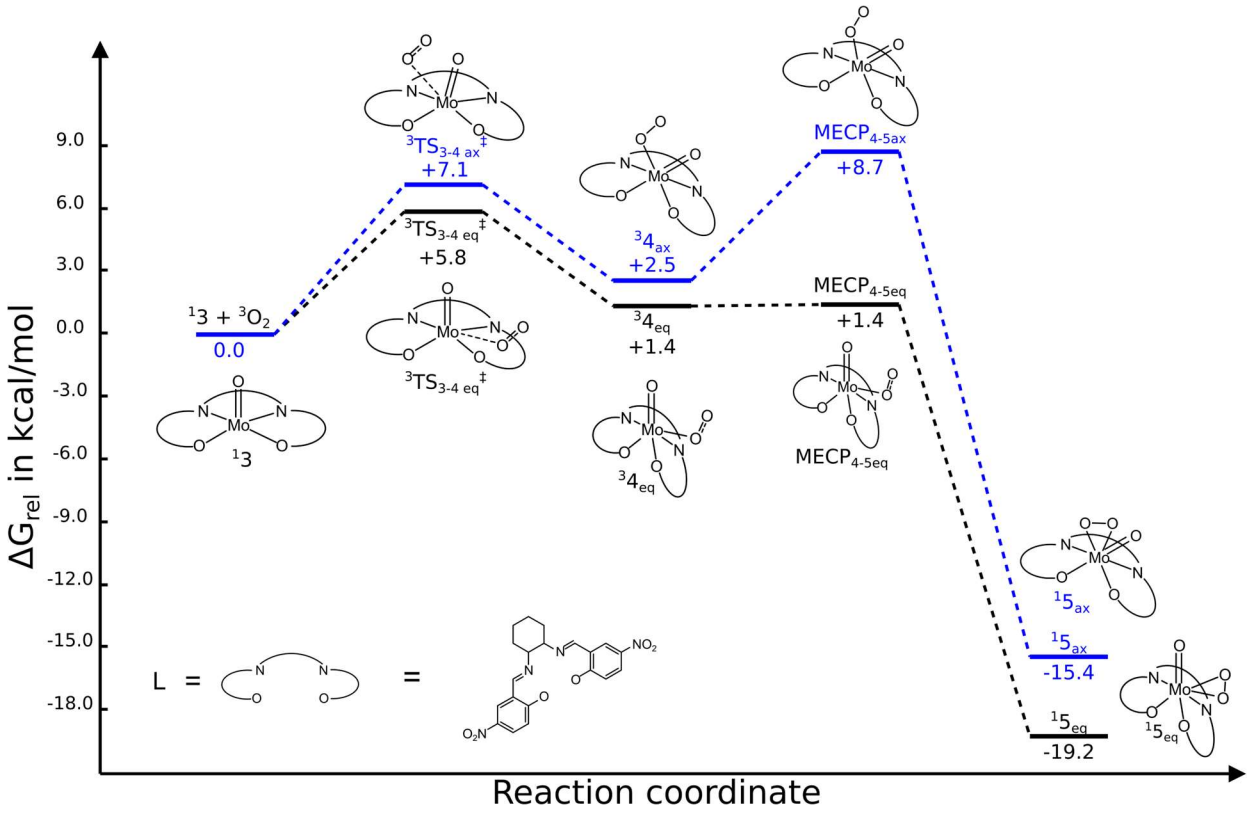

Figure 22. Reaction profile for axial (blue line) and equatorial (black line) dioxygen coordination to monooxo Mo(IV) complex **3**

B.3. *Oxygen atom transfer from molybdenum oxo-peroxo complex **5** to PMe$_3$*

The next step of the putative catalytic cycle is an oxygen atom transfer reaction, involving either the triplet oxo-superoxo molybdenum(V) molecule **4**, or the more stable singlet

oxo-peroxo molybdenum(VI) species, **5** (Figure 23). Since the oxo-superoxo species **4** was found to lie some 19 kcal above the singlet oxo-peroxo **5**, oxo-peroxo **5** is concluded to be the predominant intermediate and its reactivity with PMe_3 is our focus here. Indeed, OAT to PMe_3 by the superoxo species **4** was evaluated and found to be a uniformly higher energy process and is not discussed further.

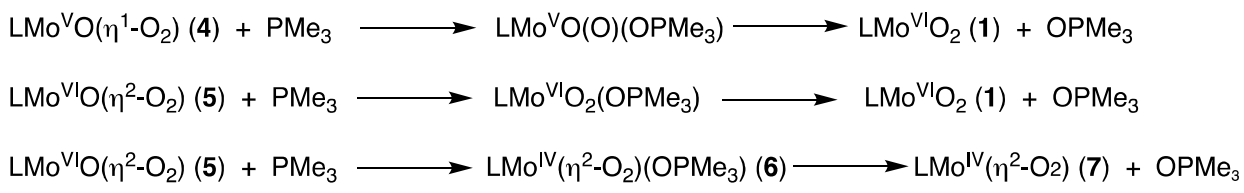

Figure 23. Oxidation of trimethyl phosphine by Mo(V) oxo-superoxo (**4**) or Mo(VI) oxo-peroxo (**5**) complexes.

The peroxo moiety often has been assumed, with limited evidence, to be more reactive toward *O*-transfer than an oxo moiety.[35] From the molybdenum(VI) oxo-peroxo complex **5** transfer of an oxygen atom from the peroxo moiety could produce (cy-salen)MoO_2 **1** directly. Isomeric singlet transition states for the approach of PMe_3 from the axial and equatorial directions were located by a two-dimensional scan along the forming P-O bond and the dissociating O-O bond (Figure 24). This atom transfer occurs with a significant change in the coordination geometry of the peroxo group, with the Mo-O2 bond length increasing dramatically, approaching η^1-binding of the dioxygen moiety, with little change in the O-O bond distance. The conversion from oxo-peroxo **5** + PMe_3 to produce dioxo complex **1** and $OPMe_3$ can be described as a concerted attack by PMe_3 with O-P bond formation and Mo-O bond breaking, but with O-O bond breaking apparently occurring later in the process. Inspection of FMO's for $\mathbf{TS_{5\text{-}1ax}}$ shows HOMO-2 (Figure 24b) with distinct P-O bonding and O-O antibonding (π^*) character (with no contribution from Mo), with forming P-O bonding and decreasing O-O bonding. The transfer of electron density to Mo as PMe_3 is added is indicated by a change in the APT atomic charges on Mo from the oxo-peroxo reactant **5** (+2.53) to the TS (+2.10). Importantly, these peroxo-based OAT transition states were found to be associated with rather high activation energies of $\Delta G^{\ddagger}_{ax}$ = 34.0 kcal/mol and $\Delta G^{\ddagger}_{eq}$ = 35.2 kcal/mol.

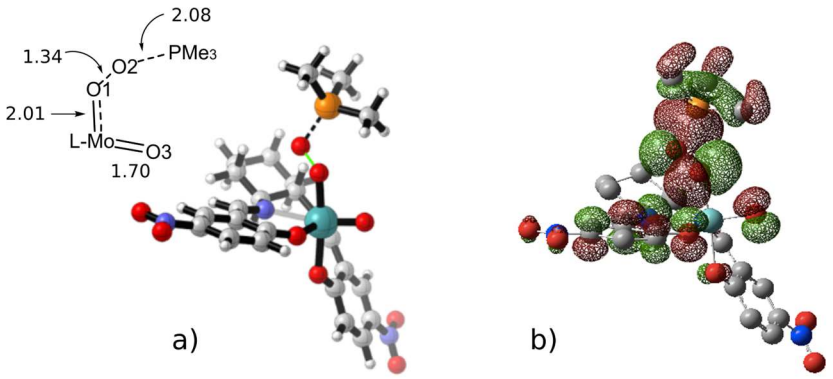

Figure 24. (a) OAT transition state from the peroxo group ^{1}**TS$_{5\text{-}1ax}$** (left); selected bond lengths (Å) are shown in the inset. (b) (HOMO-2) for ^{1}**TS$_{5\text{-}1ax}$** (right), hydrogen atoms omitted for clarity.

An alternative pathway for OAT from the oxo-peroxo complex **5** is for the oxo *O*-atom to be transferred. A transition state for the PMe_3 reaction at the oxo group of **5**, **TS$_{5\text{-}6}$**, was located by scanning on the O-P distance and optimized as shown in Figure 25b. This is a relatively early transition state, with a lengthening Mo-O(oxo) distance (1.81 Å vs. 1.71 in oxo-peroxo **5**), a relatively long bond-forming P-O distance and little change in the bond metrics within the peroxo unit. The $\Delta G^{\ddagger}$ for this OAT reaction at the oxo-group of **5** (+20.2 kcal/mol axial oxo, +21.0 kcal/mol equatorial oxo) is nearly the same as for the dioxo OAT step of **1** (+20.1 kcal/mol axial). Most significantly, the activation energy for reaction at the oxido group of **5** is substantially lower, by 12-14 kcal/mol, than for the peroxo *O*-atom attack. As for the origin of the preferred oxo-*O* attack by PMe_3 on oxo-peroxo **5**, we note that the calculated atomic charges (Mulliken or APT) for **5** are more negative on the oxo-O (-0.8) than on the peroxo-O's (-0.25, -0.35), inconsistent with the energetically preferred oxo-attack. The preference for oxo-atom attack by PMe_3 on **5** is suggested by the majority of low-lying acceptor orbitals, which have a larger coefficient on the oxo *O*-atom than on the peroxo O's (e.g. LUMO+1, Figure 25a). This suggests that the selectivity of phosphine attack on **5** is governed by maximizing orbital overlap and FMO energy matching between the electron-donor *P*-center and the electron acceptor **5**.

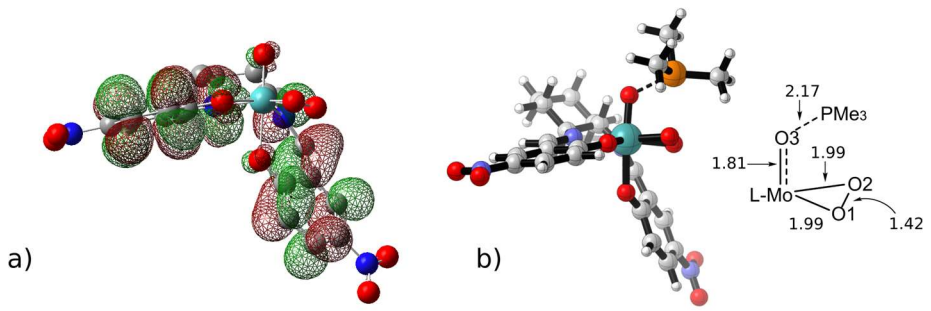

Figure 25. a) LUMO +1 for singlet (cy-salen)Mo(O)(η^2-O_2) (^{1}**5**$_{eq}$); H-atoms omitted; (b) OAT transition state structure ^{1}**TS**$_{5\text{-}6}$ for oxo atom transfer from oxo-peroxo complex **5**; selected bond lengths (Å) are shown in the inset.

The oxo-centered OAT proceeds through a ternary peroxo-Mo(IV) phosphine oxide complex, LMo(IV)(η^2-O_2)($OPMe_3$) (**6**) (Figure 26). This d^2 species may be in a high (S=1, triplet) or low (S=0, singlet) spin state. The triplet species ^{3}**6** is calculated to be stabilized by 11.0 kcal/mol relative to the singlet structure. The geometries of ^{3}**6**$_{ax}$ and ^{1}**6**$_{ax}$ are quite similar around the transferring oxo group, but the equatorial peroxo group in the triplet species displays a somewhat more unsymmetrical geometry similar to the oxo-attack singlet. Both show an increase in the O-O bond length (decreased bond order), consistent with increased back bonding from the reduced Mo(IV) center. From the oxo-peroxo species **5** the conversion to the ternary complexes ^{3}**6** and ^{1}**6** is highly exergonic, $\Delta G = -30$ kcal/mol to singlet ^{1}**6** and $\Delta G = -41$ kcal/mol to the triplet ^{3}**6**. The spin density of the triplet ternary complex ^{3}**6** is nearly entirely on the molybdenum center (1.81 e^-, Figure 26). Since ^{3}**6** is more stable than the singlet, a spin-crossover is needed to transition to the more stable triplet surface between the atom-transfer transition state ^{1}**TS**$_{5\text{-}6}$ and the ternary phosphine oxide complex ^{3}**6**. The MECP for this process was located near the crossing of the singlet and triplet surfaces at approximately -15 kcal and is shown in Figure 27. Its structural features are very similar to the precursor ternary phosphine oxide complexes ^{1,3}**6** (Figure 26a,b).

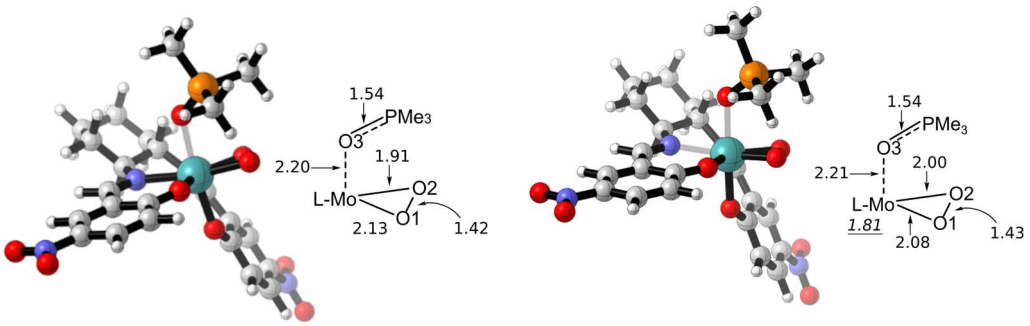

Figure 26. Ternary $OPMe_3$ complexes for OAT to the singlet oxo moiety, $^1\mathbf{6_{ax}}$ (left) and triplet, $^3\mathbf{6_{ax}}$ for oxo OAT (right); selected bond lengths (Å) are shown in the inset; atomic spin density is italicized/underlined.

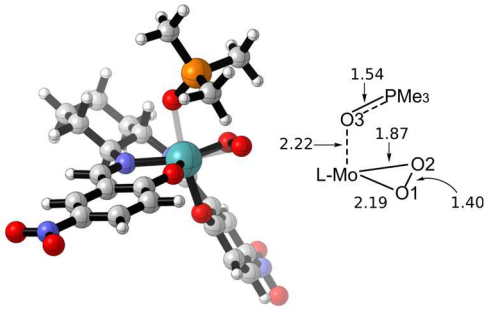

Figure 27. **MECP$_{5\text{-}6}$**; selected bond lengths (Å) are shown in the inset.

The release of phosphine oxide from ternary complex **6** was then studied to complete the favored transfer of the axial oxo atom. The transition states for this were located for the singlet and triplet species and are shown in Figure 28. The changes in geometry for the complex as the product $OPMe_3$ dissociates are quite similar to those observed for **TS$_{2\text{-}3}$**, with the peroxo ligand shifting toward the axial position and the axially ligated salicylimine ligand unit relaxing toward a square pyramidal geometry. A significant increase in the O-O bond length for the singlet species (1.48 Å) and a small increase in the triplet species may be the result of increased back-bonding from the metal to the peroxo unit by reduction of the molybdenum center. The spin density of the triplet complex is again concentrated on the molybdenum(IV) center, with little contribution from ligand atomic spin densities (Figure 28b). The activation barrier $\Delta G^{\ddagger}$ for the singlet is 16.8 kcal/mol, while that of the triplet is a somewhat higher 22.7 kcal/mol.

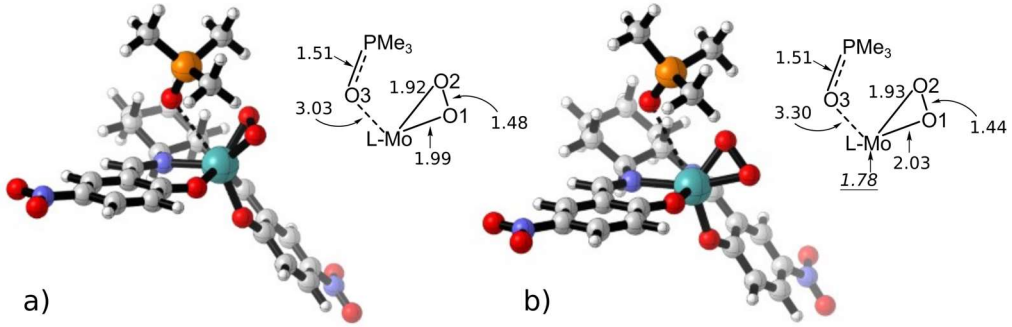

Figure 28. Transition states for dissociation of $OPMe_3$. (a) ^{1}**TS$_{6\text{-}7ax}$** from ^{1}**6**$_{ax}$; selected bond lengths (Å) are shown in the insets; (b) ^{3}**TS$_{6\text{-}7ax}$** from ^{3}**6**$_{ax}$; atomic spin densities are italicized/underlined.

Dissociation of $OPMe_3$ from (cy-salen)Mo(η^2-O_2)($OPMe_3$) **6** is modestly endergonic, yielding the distorted square pyramidal monoperoxo molybdenum(IV) complex **7** (Figure 29). The peroxo group of the triplet species ^{3}**7**, exhibits a nearly symmetrical η^2-coordination mode, while in the singlet the peroxo group is unsymmetrically bound. The O-O bond lengths of **7**, 1.43 Å, 1.45 Å, are significantly longer than in the oxo-peroxo Mo(VI) of **5**, an effect probably derived from the stronger back-bonding to the peroxo group for Mo(IV). Radical character in the triplet monoperoxo is concentrated on the molybdenum atom (spin density = 1.68) with small spin densities on the peroxo oxygen atoms, 0.09 and 0.06 (Figure 29c). Importantly, the triplet of **7** is calculated to be 9.4 kcal/mol more stable than the singlet, identifying it as the predominant ground state of the monoperoxo complex **7**.

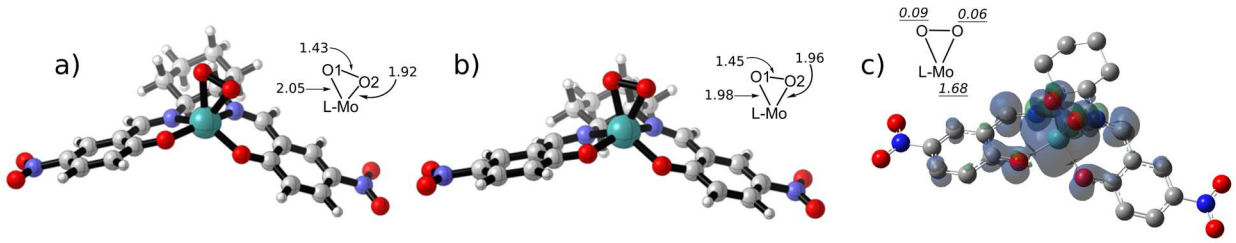

Figure 29. (a,b) B3LYP-optimized structures of the singlet (left) and the more stable triplet monoperoxo Mo(IV) complex **7** (center); selected bond lengths (Å) are shown in the inset. (c) (right) electron spin density map for the triplet monoperoxo ^{3}**7** (spin densities are italicized/underlined).

We now consider the overall energetics for the OAT stage of the phosphine oxidation. For each of the possible OAT pathways (Figure 30), the axial and equatorial coordination isomers have very similar activation barriers (superoxo $\Delta\Delta G^{\ddagger}$ = 0.75 kcal/mol, peroxo $\Delta\Delta G^{\ddagger}$ = 1.1 kcal/mol, oxo $\Delta\Delta G^{\ddagger}$ = 0.8 kcal/mol), so only the energies for the more stable isomer (usually the axial) are shown in the energy profile. Between the peroxo- and oxo-group transfer pathways, the oxo-atom transfer is found, unexpectedly, to be the lower energy process, with an activation barrier 13.7 kcal/mol lower than the peroxo-atom transfer. The peroxo group has typically been considered to be the more reactive moiety for OAT reactions,[20,35] supported by studies of sulfides and olefins with Mimoun-type complexes (Mo-oxo-diperoxo).[50,63] However, to our knowledge, this has been demonstrated to be the case for phosphine oxidation only in one oxo-*diperoxo*-Mo/H_2O_2 system.

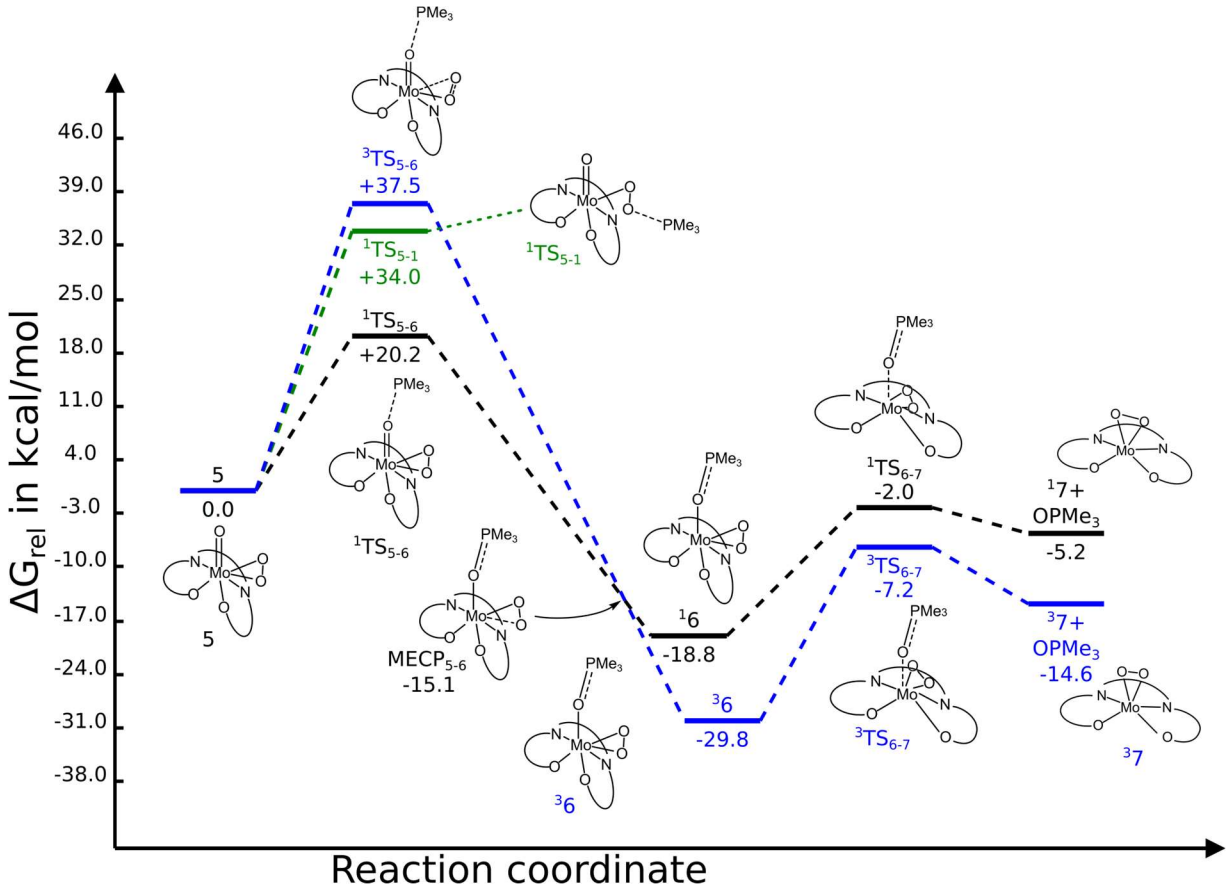

Figure 30. Reaction pathways for OAT to PMe_3 from the Mo(VI) oxo-peroxo compound **5**. Singlet pathway shown with black dashed line; triplet pathway shown with blue dashed line.

B.4. *Regeneration of (cy-salen)Mo(VI)O_2 (**1**) from (cy-salen)Mo(IV)(η^2-O_2)* (**7**)

Note that when the oxo-atom transfer to PMe_3 from the oxo-peroxo complex **5** occurs, a monoperoxo-Mo(IV) species **7** is produced. The favorability of oxo-atom transfer from the oxo-peroxo complex **5** to form a peroxo-Mo(IV) species **7** led us to consider a little precedented transformation – the splitting of the Mo(IV) peroxo group of **7** to regenerate the dioxomolybdenum(VI) complex **1**, to complete the catalytic cycle. How does this species continue on in the catalytic cycle? One can consider the conversion of a metal-monoperoxo to metal-dioxo species as a six-electron reorganization – formally a two-electron oxidation of the metal, Mo(IV) to Mo(VI), accompanied by the breaking of the O-O bond and the making of two Mo-O bonds. To explore the full profile for regeneration of the dioxo complex from the monoperoxo species, both singlet and triplet surfaces were modeled to establish the energetic viability of the possible intermediates and transition states (Figure 31).

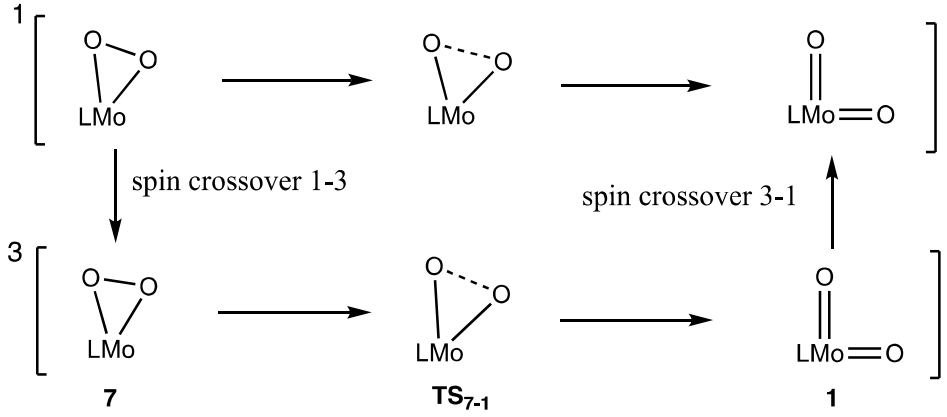

Figure 31. (top) Singlet reaction pathway for peroxo-to-dioxo splitting reaction of (cy-salen)Mo(η^2-O_2) **7** (L=cy-salen); (bottom) triplet pathway for peroxo splitting of **7**

Transition states for peroxo splitting of the monoperoxo species **7** were located by scanning along the dissociating O-O bond, then optimizing to a Berny transition state for both the singlet and triplet spin states. Proceeding from the singlet monoperoxo ^{1}**7** leads to ^{1}**TS$_{7\text{-}1}$** (Figure 32a), which has a substantially lengthened O-O distance (1.88 Å) relative to the

monoperoxo precursor ^{1}**7** (1.43 Å) and a pronounced difference in the two Mo-O bond lengths, Mo-O(ax) 1.75 Å vs Mo-O(eq) 2.01 Å. This is indicative of significant O-O bond-breaking with compensating Mo-O bond-making largely in one Mo-O moiety (c.f. 1.72 Å for oxo-complex $LMoO_2$).[4] The Mulliken charges of the two O-atoms in ^{1}**TS**$_{7\text{-}1}$ are also significantly different, with the equatorial oxygen carrying greater negative charge (-0.44) than the axial (-0.39). Consistent with the increased polarity of the singlet transition state is a solvent stabilization effect ($\Delta E^{\ddagger}$ = 17.5 kcal/mol, $\Delta G^{\ddagger}$ = 10.5 kcal/mol) revealed by the M06 (tetrachloroethane solvent) energy. The O-O and Mo-O bonding changes are also visually manifested in the frontier MOs associated with the TS. For example, the HOMO for ^{1}**TS**$_{7\text{-}1}$ (Figure 33a) has strong Op - Op σ* and unsymmetrical Mo-O bonding character. The conversion from singlet peroxo intermediate ^{1}**7** via ^{1}**TS**$_{7\text{-}1}$ to the dioxo $LMoO_2$ product **1** is best described as a concerted, but asynchronous electronic process judging from the intrinsic reaction coordinate (IRC) scan (SI). The activation energy for the peroxo-to-dioxo splitting via the singlet ^{1}**TS**$_{7\text{-}1}$ is a moderate 19.9 kcal/mol.

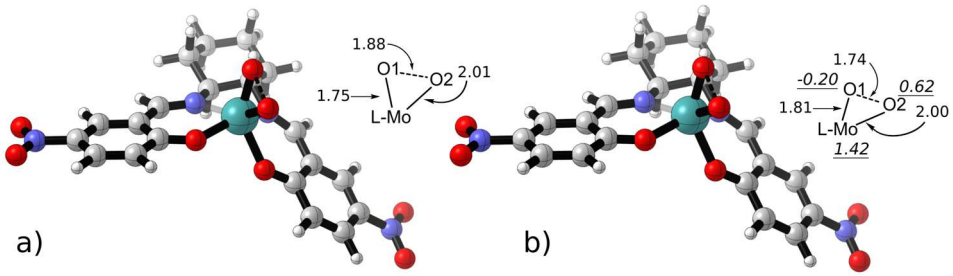

Figure 32. Peroxo splitting transition states: (a) ^{1}**TS**$_{7\text{-}1}$ (left) and (b) ^{3}**TS**$_{7\text{-}1}$ (right); selected bond lengths (Å) are shown in the inset, spin densities are underlined/italicized.

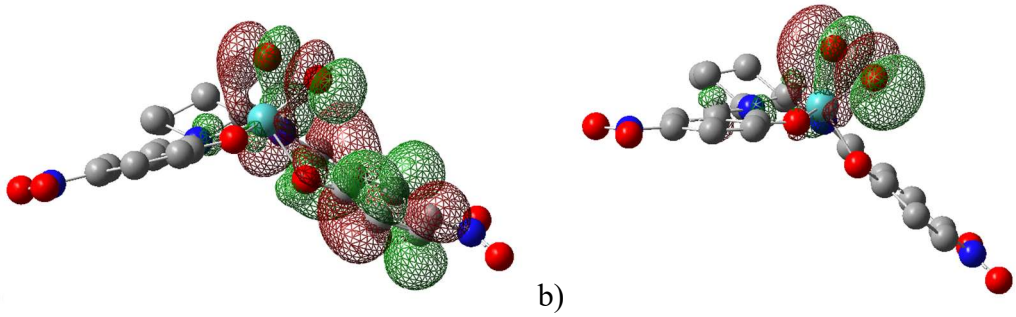

a) b)

Figure 33. (a) HOMO for ^{1}**TS**$_{7\text{-}1}$ of singlet peroxo-splitting reaction; (b) HOMO for the peroxo-splitting transition state ^{3}**TS**$_{7\text{-}1}$; H-atoms omitted for clarity.

The triplet splitting transition state ^{3}**TS**$_{7\text{-}1}$ (Figure 32b), like the singlet ^{1}**TS**$_{7\text{-}1}$, displays substantial O-O bond breaking, O-O 1.74 Å (vs 1.45 Å in mono-peroxo intermediate ^{3}**7**), and a somewhat unsymmetrical MoO_2 unit with Mo-O(51) at 1.81 Å, closer to a Mo-O double bond length, and Mo-O(44) at 1.99 Å, near to a Mo-O single bond. The electronic asymmetry of the MoO_2 unit is further reflected in the distribution of atomic charges and spin densities: APT atomic charges: Mo +1.52, O(51) -0.16, O(44) -0.24; spin densities: Mo +1.22, O(51) -0.20, O(44) +0.62. The bonding changes occurring in the TS are also manifested in the frontier MOs, most easily seen in the HOMO (Figure 33b), showing O-O antibonding and Mo-O bonding character. The IRC for the triplet TS (in SI) is also continuous from the reactant-like triplet peroxo to product-like triplet dioxo. The peroxo splitting process may then also be described as concerted, asynchronous with different timing of Mo-O bond formation. The calculated activation energy for the triplet peroxo splitting is 11.9 kcal/mol, considerably lower than for the singlet TS, which puts the triplet peroxo and the triplet TS lower in energy than the corresponding singlet species. Thus, a spin-crossover from the triplet to the singlet surface is needed subsequently to access the strongly stabilized singlet dioxo product **1** (*vide infra*).

Formation of the stable singlet dioxo complex **1** from the triplet ^{3}**TS**$_{7\text{-}1}$ is hugely exergonic (Figure 35, *vide infra*), but requires a spin crossover event. The structural parameters and energy of the optimized **MECP**$_{7\text{-}1}$ (Figure 34c) are similar to the high energy triplet dioxo product ^{3}**1**, both having substantially different Mo-O bond orders than the singlet dioxo complex **1** and may be best described as oxo-oxyl species (Figure 34 b,c). **MECP**$_{7\text{-}1}$ has more polar character than ^{3}**1**, resulting in a greater solvent stabilization effect from the M06/solvent calculation, which may account for the abnormal ordering of free energies in the reaction profile

(Figure 35). Reformation of the very stable dioxo species **1** provides the thermodynamic driving forces for this step.

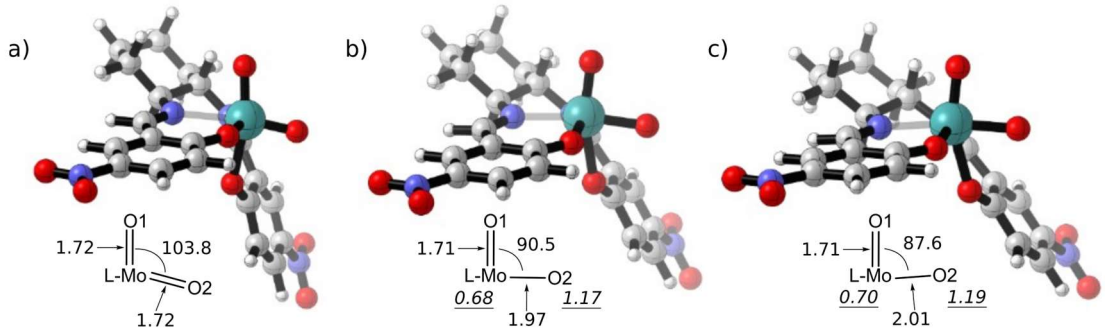

Figure 34. Computed structures of (cy-salen)MoO_2 singlet **1** (a), triplet ^{3}**1** (b), and **MECP**$_{7\text{-}1}$ (c); selected bond lengths (Å) and angles (°) are shown in the insets, atomic spin densities are underlined/italicized.

The reaction profile for the peroxo splitting reaction from the Mo(IV) monoperoxo intermediate **7** to regenerate the dioxo catalyst **1** is presented in Figure 35. Key points are the preferred lower energy pathway of the triplet species ^{3}**7** through a concerted asynchronous opening of the Mo(O-O) unit with a modest activation barrier of 11.9 kcal/mol, followed by spin crossover via **MECP**$_{7\text{-}1}$ to dioxo complex **1**.

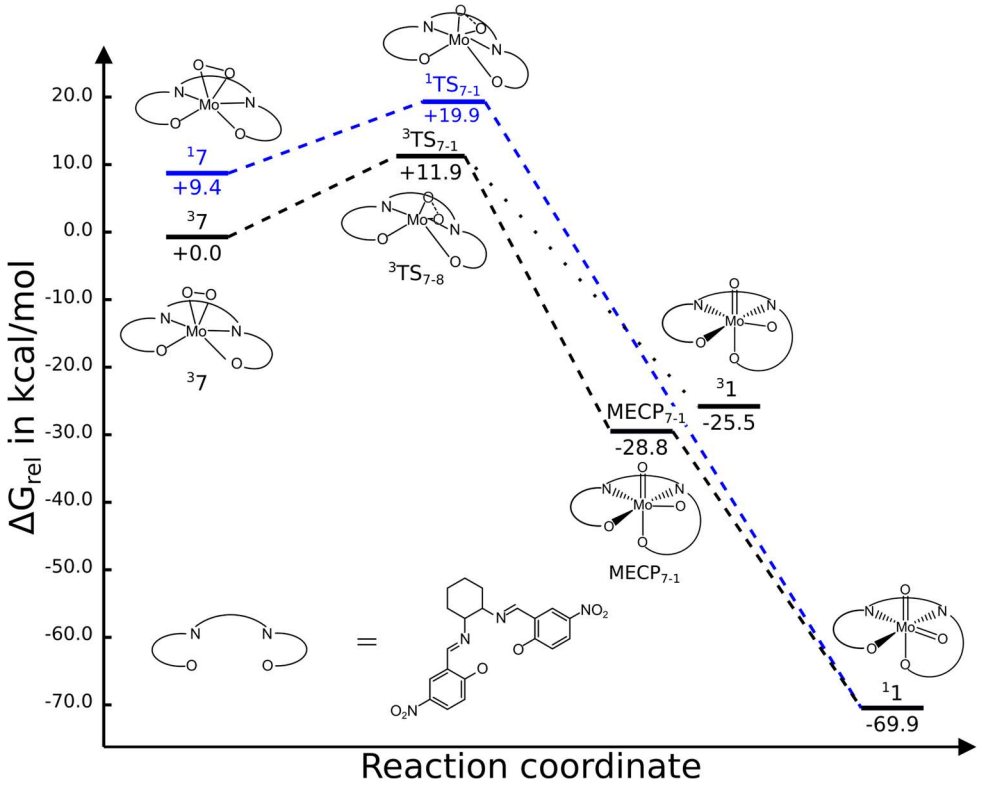

Figure 35. Reaction profile for the peroxo splitting phase of the reaction, **7** to **1**; singlet pathway shown in blue and triplet pathway in black.

Some complexes of reduced metal ions react with dioxygen to produce oxo-metals by a bimetallic Mars-Van Krevelen type pathway, leading to one atom of oxygen added to each participating metal center.[31–34,64] However, single metal-centered peroxo group splitting as per Figure 31 has also been suggested and supported computationally by Theopold and coworkers in the conversion of a putative peroxo intermediate, d^5 LCr(III)(η^2-O_2) to the dioxo derivative LCr(V)O_2.[65] Earlier, Mayer and coworkers provided evidence that a putative d^2 peroxo intermediate, (TPB)Re(O)(η^2-O_2), forms the d^0 trioxo product (TPB)ReO_3 by a bimetallic pathway, rather than the unimolecular process.[64] In a yet unpublished study in our group of the thermal and photodissociation of dioxygen from the diperoxo complex (TPP)Mo(η^2-O_2)$_2$ (→ (TPP)MoO_2 and O_2), we have also found that the splitting of the putative monoperoxo intermediate (POR)Mo(IV)(η^2-O_2) is viable via a concerted, asynchronous process with a moderate (19 kcal/mol) energy barrier.[66] The reverse transformation, i.e. metal-dioxo to –peroxo conversion, has been suggested to be operative unimolecularly in the photodecomposition of permanganate (with dioxygen evolution).[67] Based on the computational analysis presented here,

we suggest that conversion of the intermediate monoperoxo-species (cy-salen)Mo(η^2-O_2) (**7**) to (cy-salen)MoO_2 (**1**) can also occur by a low barrier concerted, asynchronous process.

B. 5. *Potential Regeneration of (cy-salen)MoO_2 (**1**) from (cy-salen)Mo(η^2-O_2) (**5**).*

Finally, we consider an alternative, somewhat more precedented pathway for conversion of the oxo-superoxo intermediate **4** to the Mo-dioxo **1**, i.e. via the bimetallic Mars-van Krevelen pathway (Figure 36). It would proceed by combining the Mo(V) oxo-superoxo species ^{1}**5** with the Mo(IV) monooxo **3** (generated from PMe_3 deoxygenation of dioxo **1**) to form the bimetallic peroxo complex **9**. Splitting of the bimetallic peroxo species via O-O bond cleavage would regenerate the original dioxo-pre-catalyst **1**. This process, if operative, would avoid PR_3 attack on the intermediate oxo-peroxo **5** entirely. We first optimized the bimetallic peroxo species **8** as the triplet; the resulting structure is shown in Figure 37. The bridged peroxo species **8** has an *anti* conformation of the Mo-O-O-Mo unit (dihedral angle=178°), as has often been seen for other bimetallic η^1,η^1-peroxo derivatives and organic peroxides.[68–70] It is symmetrical around the bridging dioxygen moiety, with an O-O bond length (1.42 Å), comparable to the peroxo group of the monometallic oxo-peroxo Mo(VI) species **5** and marginally shorter than in the Mo(IV) monoperoxo complex **7**. A singlet peroxo species ^{1}**8** appears to be unstable, since attempts to optimize it lead to O-O bond dissociation. A transition state for the association of the superoxo and mono-oxo species could be located (Figure 37) by scanning the Mo-O distance; **$TS_{3,4\text{-}8}$**, features an unsymmetrical combination of the two fragments with one long Mo-O (2.92 Å), a short Mo-O (2.16 Å) and an O-O length similar to that of superoxo-Mo species ^{3}**4**. **$TS_{3,4\text{-}8}$** is thus best described as an early transition state. The activation energy for the association of **3** and **4** to form bridged peroxo **8** via **$TS_{3,4\text{-}8}$** is a moderate 8.0 kcal/mol, while the net energy for the combination of **3** and **4** to form **8** is -16.7 kcal/mol with formation of the O-O bond.

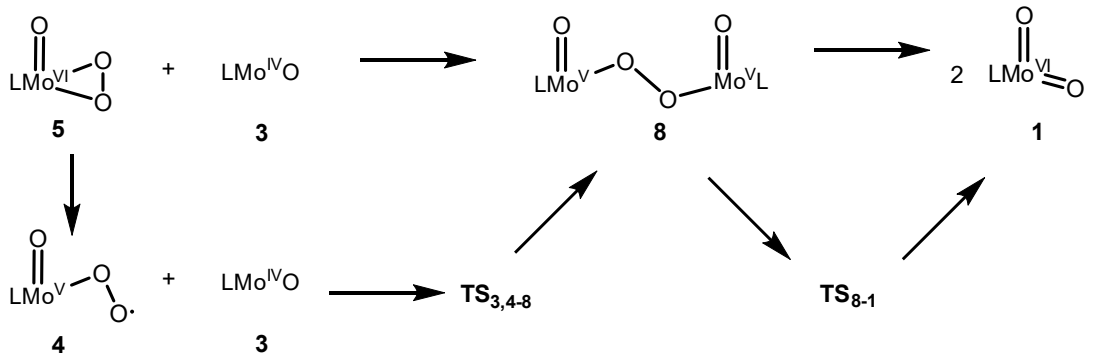

Figure 36. Mars-van Krevelen pathway for conversion of oxo-peroxo complex **5** to dioxo complex **1**

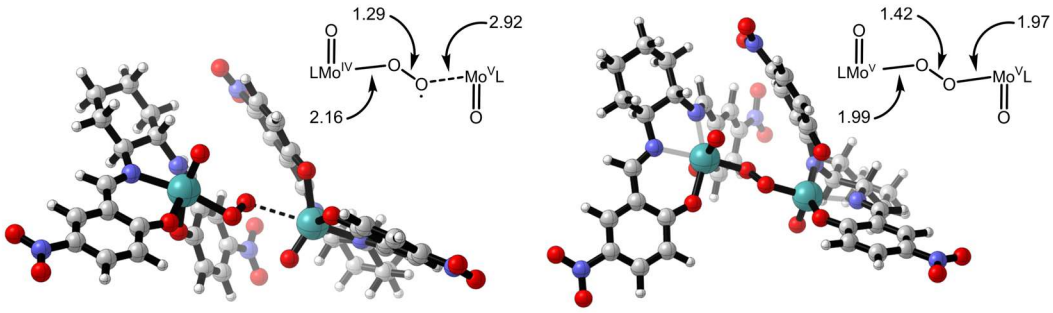

Figure 37. Transition state (left) **TS3,4-8** for formation of the bi-metallic peroxo intermediate **8** (right); selected bond lengths (Å) are shown in the insets.

The transition state search for the O-O scission of **8** to afford the dioxo-Mo (**1**) began with a O-O distance scan followed by optimization at the energy maximum. The resulting transition state **TS8-1** (Figure 38) retains the *anti* conformation of the Mo-O-O-Mo unit (dihedral =178 º), but with a considerably longer O-O distance of 1.76 Å relative to the peroxo precursor **8** (1.42 Å). An IRC scan (not shown) from **TS8-1** shows a smooth (continuous) energy profile for conversion from the reactant-like peroxo species **8** to two triplet product-like $LMoO_2$ fragments. Interestingly, the spin density and atomic charges in the triplet **TS8-1** are unsymmetrically distributed in the Mo-O-O-Mo unit: APT charges- Mo +2.26, 2.77; O -1.14, +0.25; spin densities- Mo 0.81, 0.54; O -0.13, +0.67. This suggests a polar character for the O-O bond-breaking, tending toward a $LMo(O)O^+$, $LMo(O)O^-$ ion-pair. Comparing the energy of **8** vs the

transition state gives a moderate activation energy for the O-O cleavage of 13.1 kcal. Since the transit from this triplet TS would proceed to form two (cy-salen)MoO_2 species in the triplet state (^{3}**1**), a triplet/singlet spin transition to form the stable, singlet dioxo-Mo **1** would be needed. This MECP was not located but is assumed to have a low barrier given the high exergonicity of the conversion of **8** to **1** (-73 kcal/mol).

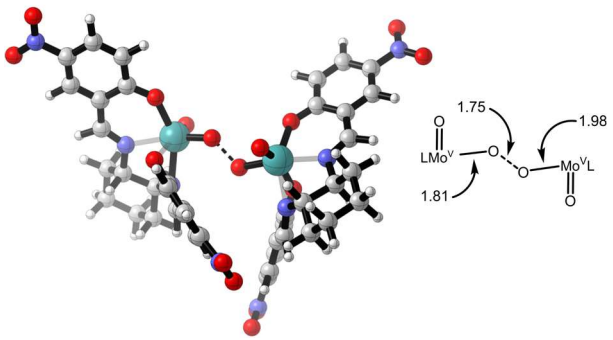

Figure 38. Transition state ^{3}**TS$_{8\text{-}1}$** for O-O cleavage of peroxo complex **8**; selected bond lengths (Å) are shown in the inset.

The total activation barrier of approximately 27 kcal/mol for combining oxo-peroxo species **5** and mono-oxo complex **3** to give the bimetallic peroxo complex **8** (Figure 39) surpasses the barriers for PMe_3 attack on the dioxo and oxo-peroxo species, **1** and **5** respectively (ca. 20 kcal/mol) and that for $OPMe_3$ dissociation from **6** (23 kcal/mol) (*vide infra*). Hence the bimetallic Mars-van Krevelen process is expected to be a minor contributor to the overall catalytic pathway. Moreover, the combination of Mo-superoxo (**3**) and Mo-monooxo (**4**) species for this Mars-van Krevelen pathway requires the association of two low concentration (high E) intermediates under steady state catalytic conditions, which would further diminish the rate through this channel. The energetic barriers for the formation and splitting of the peroxo linkage by the monometallic pathway via η^2-peroxo complex **7** (ca. 20 kcal) vs. the bimetallic pathway via **8** (27 kcal/mol) show that the monometallic pathway is favored and should constitute the main path of the catalytic reaction.

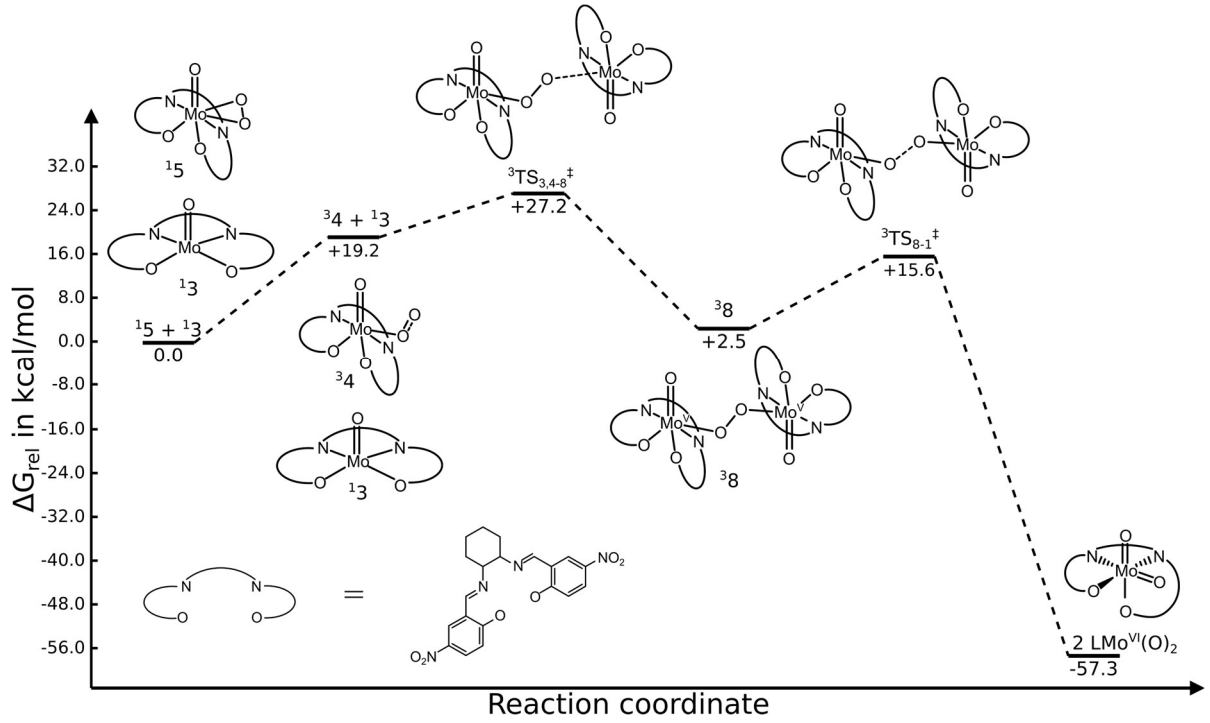

Figure 39. Energy profile for the bimetallic dioxygen cleavage via peroxo complex **8**.

B.5. The complete energy profile for the aerobic (cy-salen)MoO_2-catalyzed oxidation of PMe_3

The complete energy profile for the catalytic pathway that includes the lowest energy intermediates and transition states is illustrated in Figure 40. The thermodynamic driving force for each regime of the reaction is the formation of oxygen-containing double-bonded moieties, namely the phosphine oxide and the regenerated dioxomolybdenum complex **1**. The intermediate regimes are fairly thermoneutral, with the spin crossovers to stabilized triplet species as the next largest thermodynamic sinks. It can be seen here that the highest kinetic barriers are associated with three steps: transfer of an oxido-O to PMe_3 from the dioxo species **1** and from the oxo-peroxo complex **5** and Me_3PO dissociation from the monoperoxo complex **7**. The activation barriers for these three steps are quite similar, 20-25 kcal/mol. The experimental consequences of this feature could result in a complex rate dependency on the phosphine, oxygen and phosphine oxide concentrations. Additionally, the relatively lower barrier (11.9 kcal/mole) for the Mo(IV)-monoperoxo to Mo(VI)-dioxo conversion (**^{3}7 → 1**) suggests that this stage of the cycle would be kinetically and experimentally undetectable under the catalytic reaction conditions. The

Hammett correlation for the set of *para*-substituted catalysts observed experimentally, with increasing rate associated with the more electron deficient complexes, is accounted for by the electronic character of the nucleophilic phosphine attack on the electrophilic oxo-Mo(VI) centers. Energetic analysis of the potential Mars-van Krevelen shunt between oxo-peroxo complex **5**, bridged peroxo species **8**, and the dioxo complex **1** indicates that this process is unlikely to contribute significantly to the main catalytic pathway.

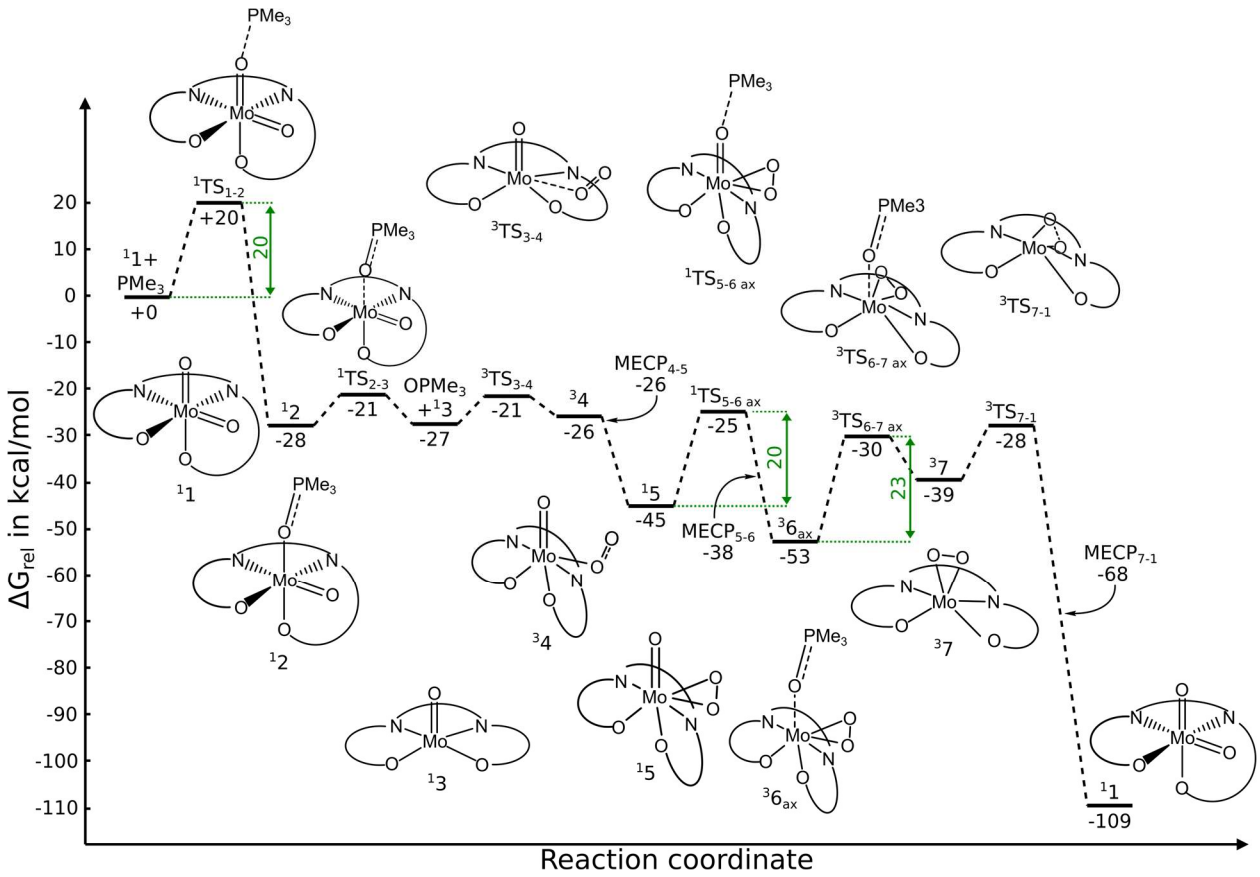

Figure 40. The complete minimum energy reaction profile for aerobic oxidation of PMe_3 catalyzed by (cy-salen)MoO_2 (**1**).

Our computational study indicates that the second oxidation step does not proceed via OAT from the peroxo group, as reported by Sharpless, et al. for oxidation of phosphines by oxo-*diperoxo* molybdenum complexes,[35] but rather through transfer of the oxo atom of the oxo-peroxo species **5**. This means that the overall reaction proceeds through OAT from the dioxomolybdenum species **1**, followed by coordination of dioxygen to form the oxo-superoxo

species **4** and its crossover-stabilized singlet oxo-peroxo sibling. The second oxygen atom transfer of the catalytic cycle proceeds most favorably via phosphine attack on the remaining oxo group of **5**, and the product monoperoxo molybdenum(IV) complex **7** then splits the peroxo moiety, rearranging to form the initial dioxo complex **1**.

Three steps in the overall energy profile of Figure 40 have comparably high energy barriers (20-23 kcal/mol), which would contribute most to determine the overall reaction rate; these are: **1** + PMe_3 → **2**, ΔG^*=20 kcal; **5** + PMe_3 → **6**, ΔG^*=20 kcal; and **6** → **7** + $OPMe_3$, ΔG^*=23 kcal. Since each of these steps involve the phosphine or its oxide, it is appropriate to consider the likely differences between the experimental reactions with PPh_3 vs. the modeled reaction with PMe_3. Our calculation for the **1** + PPh_3 → **2** reaction showed a small increase in ΔG^* to 22.5 kcal (vs. 20.0 kcal for the PMe_3 reaction). Although it was not calculated, the similar electronic nature of the **5** + PR_3 → **6** step allows us to estimate a comparably small (1-2 kcal) increase in its $\Delta G^{\ddagger}$ for PPh_3 relative to PMe_3. Finally, for the **6** → **7** + OPR_3 conversion, we estimate a rather small difference in the activation energies for $OPPh_3$ vs $OPMe_3$. With the less basic, more sterically encumbered $OPPh_3$ leaving group we predict a slightly smaller activation energy, e.g. 20-22 kcal, relative to that calculated for $OPMe_3$ (23.0 kcal/mol). Hence, we conclude that while the there are likely small changes in the PR_3-involved energy barriers between the experimental reactions with PPh_3 and those modeled with PMe_3, the preferred (lowest energy) catalytic pathway will remain the same regardless of the phosphine. The essential features of this pathway are summarized in Figure 41: 1) OAT from $LMoO_2$ to phosphine; 2) dioxygen coodination to LMoO to form oxo-peroxo intermediate $LMoO(\eta^2\text{-}O_2)$; 3) selective oxo-atom transfer from the latter to phosphine; and 4) novel peroxo splitting of $LMo(\eta^2\text{-}O_2)$ to regenerate $LMoO_2$.

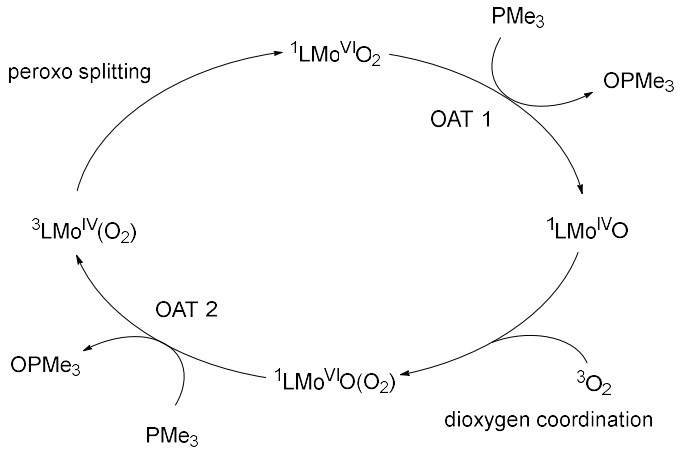

Figure 41. Simplified, most energetically favorable pathway for (cy-salen)Mo(VI)O_2-catalyzed aerobic oxidation of PMe_3.

C. Conclusions

The ability of a set of (cy-salen)MoO_2 complexes to catalyze the aerobic oxidation of PPh_3 has been demonstrated experimentally and the effects of changing the electronic character of the catalyst on oxidation rate have been established. DFT computational investigation of the catalytic pathway for the aerobic oxidation of PMe_3 catalyzed by (cy-salen)MoO_2 (**1**) supports the following sequence as the lowest energy process (Figure 41): 1) associative addition of PMe_3 to an oxo-O of $LMoO_2$ to give LMo(IV)(O)($OPMe_3$) (**2**); 2) $OPMe_3$ dissociation from **2** to produce LMo(IV)O; 3) stepwise O_2 association with the latter to form the oxo-peroxo species LMo(VI)(O)(η^2-O_2) **5** via a superoxo LMo(V)(O)(η^1-O_2) intermediate **4**; 4) *O*-transfer reaction of PMe_3 with oxo-peroxo species **5** occurs preferentially at the oxo-group, rather than the peroxo unit leading, after $OPMe_3$ dissociation, to the reduced peroxo species LMo(IV)(η^2-O_2) **7**; 5) transformation of the more stable triplet peroxo species ^{3}**7** to the starting pre-catalyst LMo(VI)O_2 (**1**) via a concerted, asynchronous electronic isomerization and attendant spin-crossover with moderate barriers.

D. Experimental Section

D.1. General procedure for preparation of ligands and (cy-salen)MoO_2 (1a-e)

The cy-salen ligands were prepared by combining 2 equivalents of the respective salicylaldehyde with the diamine in alcoholic solution and heating at reflux, as reported previously.[4] The ligands were isolated by filtration and combined with an equimolar amount of dioxomolybdenum bisacetylacetonate, $MoO_2(acac)_2$, in chlorinated solvent (TCE or chlorobenzene) and heated at reflux for 4h. The reaction mixture was concentrated and the product complex isolated by filtration.[4]

D.2. Phosphine oxidation- catalyst variation study

To a round bottom flask was added 183 mg (0.69 mmol) of triphenylphosphine, 10 mL of chlorobenzene, and approximately 1 mol% catalyst (5.3 mg **1**, 98 μmol; 3.1 mg **4**, 69 μmol; 3.8 mg **5**, 70 μmol; 4.7 mg **6**, 70 μmol; or 3.6 mg **7**, 70 μmol), along with a stir bar. The reaction flasks were then purged with O_2 before being capped and placed in a 50°C oil bath for 4 hours. Aliquots were taken from each reaction mixture and the conversion was determined by ^{31}P NMR integration.

D.3. Phosphine oxidation- turnover study under dioxygen atmosphere

To a round bottom flask was added chlorobenzene (20 mL), 2.5 mg complex **2** (3.5 μmol), and triphenylphosphine (671.5 mg, 2.5 mmol). The flask was evacuated and backfilled with O_2 before being placed in an oil bath at 50°C. Aliquots were withdrawn periodically to determine progress of the reaction by ^{31}P NMR spectral integration.

D.4. Phosphine oxidation- dioxygen concentration study

To each of eight 13 mm culture tubes was added 12.0 mg triphenylphosphine (0.045 mmol) and 0.7 mL chlorobenzene. Half of the tubes were then charged with a small portion (~0.2 mg, 0.4 μmol) of complex **1**, the other tubes serving as blank reactions. The catalyzed and

blank reactions were then capped with a septum and assigned pairwise to one of four conditions: 1) capped under ambient pressure, 2) atmospheric pressure of air maintained by way of a balloon, 3) atmospheric pressure of air maintained by a balloon, with stirring, and 4) 1 atmosphere of O_2 maintained by balloon. For condition 4, the culture tube was sparged with oxygen gas prior to capping with a septum. All reactions were then placed in a 60°C oil bath and incubated overnight. The percent conversion was determined by ^{31}P NMR integration.

D.5. Computational methods

All calculations were carried out using Gaussian 09. Structures were optimized using the B3LYP hybrid functional and the basis sets: Mo, LANL2DZ; P, S, 6-311++G(d,p); C, H, O, N, 6-311 G(d) using Gaussian 09's ultrafine integration grid. Solvent phase energies were obtained as a single point energy calculation using the M06 functional (basis sets: Mo, SDD; P, S, C, H, O, N, 6-311++G(d,p)) in conjunction with the SMD solvent model[71] for 1,2-dichloroethane. The free energy correction to the energy was taken from the B3LYP frequency calculation. Relaxed coordinate scans were employed to guide Berny saddle point searches. For transition states $\mathbf{TS_{2\text{-}3}}$ and $\mathbf{TS_{3\text{-}4}}$, starting points for the Berny optimizations were located by running a series of single-point optimizations with the M-OA bond length frozen. Transition states were verified by the existence of a single imaginary frequency along the reaction coordinate involving bond making/breaking and with smooth intrinsic reaction coordinate (IRC) plots. Minimum-Energy Crossing Point (MECP) structures were calculated using the B3LYP optimized singlet and triplet structures as inputs for the sobMECP optimization algorithm[62] and free energies for these structures were computed from Gaussian frequency calculation outputs. Reaction profiles were generated using the mechaSVG program.[72]

Acknowledgements. K.N. and T.R. are grateful for support from the Oklahoma Supercomputer Center for Education and Research (OSCER) and from an A. C. Cope Scholar Award to K.N. C.L. was supported in part by the NSF (CHE2102071). We also thank Profs. Yihan Shao and Daniel Glatzhofer for insightful and helpful discussions.

References

(1) Hille, R.; Hall, J.; Basu, P. The Mononuclear Molybdenum Enzymes. *Chem. Rev.* **2014**, *114*, 3963–4038.

(2) Hille, R. The Molybdenum Oxotransferases and Related Enzymes. *Dalton Trans.* **2013**, *42*, 3029–3042.

(3) Sanz, R.; Pedrosa, M. Applications of Dioxomolybdenum(VI) Complexes to Organic Synthesis. *Curr. Org. Synth.* **2009**, *6*, 239–263.

(4) Rusmore, T. A.; Behlen, M. J.; John, A.; Glatzhofer, D. T.; Nicholas, K. M. Oxidative Kinetic Resolution of *P*-Chiral Phosphines Catalyzed by Chiral (Salen)Dioxomolybdenum Complexes. *Mol. Catal.* **2021**, *513*, 111776–111776.

(5) Harlan, E. W.; Berg, J. M.; Holm, R. H. Thermodynamic Fitness of Molybdenum(IV,VI) Complexes for Oxygen-Atom Transfer Reactions, Including Those with Enzymic Substrates. *J. Am. Chem. Soc.* **1986**, *108*, 6992–7000.

(6) Choplin, F.; Kaufmann, G.; Rohmer, R. Vibrational Spectra of New Coordination Complexes of Molybdenum(VI) with Trimethylamine and Trimethylarsine Oxides. *C R Acad Sc Paris Ser. C* **1969**, *268*, 333–336.

(7) Holm, R. H. Metal-Centered Oxygen Atom Transfer Reactions. *Chem. Rev.* **1987**, *87*, 1401–1449.

(8) Holm, R. H.; Donahue, J. P. A Thermodynamic Scale for Oxygen Atom Transfer Reactions. *Polyhedron* **1993**, *12*, 571–589.

(9) Nemykin, V. N.; Basu, P. Oxygen Atom Transfer Reactivity from a Dioxo-Mo(VI) Complex to Tertiary Phosphines: Synthesis, Characterization, and Structure of Phosphoryl Intermediate Complexes. *Inorg. Chem.* **2005**, *44*, 7494-7502

(10) Whiteoak, C. J.; Britovsek, G. J. P.; Gibson, V. C.; White, A. J. P. Electronic Effects in Oxo Transfer Reactions Catalysed by Salan Molybdenum(vi) Cis-Dioxo Complexes. *Dalton Trans.* **2009**, No. 13, 2337–2337.

(11) Hazell, A.; McKenzie, C. J.; Nielsen, L. P.; Schindler, S.; Weitzer, M. Mononuclear Non-Heme Iron(III) Peroxide Complexes: Syntheses, Characterisation, Mass Spectrometric and Kinetic Studies. *J. Chem. Soc. Dalton Trans.* **2002**, No. 3, 310–317.

(12) Yee, G. M.; Tolman, W. B. Transition Metal Complexes and the Activation of Dioxygen. In *Sustaining Life on Planet Earth: Metalloenzymes Mastering Dioxygen and Other Chewy Gases*; Kroneck, P. M. H., Sosa Torres, M. E., Eds.; Metal Ions in Life Sciences; Springer International Publishing: Cham, 2015; pp 131–204.

(13) Würtele, C.; Gaoutchenova, E.; Harms, K.; Holthausen, M. C.; Sundermeyer, J.; Schindler, S. Crystallographic Characterization of a Synthetic 1:1 End-On Copper Dioxygen Adduct Complex. *Angew. Chem. Int. Ed.* **2006**, *45*, 3867–3869.

(14) Fujisawa, K.; Tanaka, M.; Moro-oka, Y.; Kitajima, N. A Monomeric Side-On Superoxocopper(II) Complex: $Cu(O_2)(HB(3\text{-}^tBu\text{-}5\text{-}IPrpz)_3)$. *J. Am. Chem. Soc.* **1994**, *116*, 12079–12080.

(15) Reynolds, A. M.; Gherman, B. F.; Cramer, C. J.; Tolman, W. B. Characterization of a 1:1 $Cu{-}O_2$ Adduct Supported by an Anilido Imine Ligand. *Inorg. Chem.* **2005**, *44*, 6989–6997.

(16) Lewis, E. A.; Tolman, W. B. Reactivity of Dioxygen−Copper Systems. *Chem. Rev.* **2004**, *104*, 1047–1076.

(17) Bakac, A. Oxygen Activation with Transition-Metal Complexes in Aqueous Solution. *Inorg. Chem.* **2010**, *49*, 3584–3593.

(18) Punniyamurthy, T.; Velusamy, S.; Iqbal, J. Recent Advances in Transition Metal Catalyzed Oxidation of Organic Substrates with Molecular Oxygen. *Chem. Rev.* **2005**, *105*, 2329–2364.

(19) Zhu, Z.; Espenson, J. H. Methylrhenium Trioxide as a Catalyst for Oxidations with Molecular Oxygen and for Oxygen Transfer. *J. Mol. Catal. Chem.* **1995**, *103*, 87–94.

(20) Dupé, A.; Judmaier, M. E.; Belaj, F.; Zangger, K.; Mösch-Zanetti, N. C. Activation of Molecular Oxygen by a Molybdenum Complex for Catalytic Oxidation. *Dalton Trans.* **2015**, *44*, 20514–20522.

(21) Tachibana, J.; Imamura, T. New Dioxygen Complex of Molybdenum Porphyrin. Reactions of Oxomolybdenum(IV) Porphyrins with Molecular Oxygen. *Chem. Lett.* **1990**, *19*, 2085–2088.

(22) Fujihara, T.; Hoshiba, K.; Sasaki, Y.; Imamura, T. Reversibility in the Formation of Oxo(Peroxo)Porphyrinatomolybdenums. *Bull. Chem. Soc. Jpn.* **2000**, *73*, 383–390.

(23) Tachibana, J.; Imamura, T.; Sasaki, Y. Synthesis and Characterization of a Novel Dioxygen Complex of Molybdenum Porphyrin. *J. Chem. Soc. Chem. Commun.* **1993**, No. 18, 1436–1438.

(24) Nagase, K.; Hasegawa, U.; Kohori, F.; Sakai, K.; Nishide, H. The Photoresponse of a Molybdenum Porphyrin Makes an Artificial Gill Feasible. *J. Membr. Sci.* **2005**, *249*, 235–243.

(25) Wagnerová, D. M.; Lang, K. Photorelease of Triplet and Singlet Oxygen from Dioxygen Complexes. *Coord. Chem. Rev.* **2011**, *255*, 2904–2911.

(26) Das, S.; Bhowmick, T.; Punniyamurthy, T.; Dey, D.; Nath, J.; Chaudhuri, M. K. Molybdenum(VI)-Peroxo Complex Catalyzed Oxidation of Alkylbenzenes with Hydrogen Peroxide. *Tetrahedron Lett.* **2003**, *44*, 4915–4917.

(27) Bruno, S. M.; Amarante, T. R.; Almeida Paz, F. A.; Pillinger, M.; Valente, A. A.; Goncalves, I. S. Oxidation of Sulfides in Aqueous Media Catalyzed by Pyrazole-Oxidoperoxido-Molybdenum(VI) Complexes. *Inorg. Chim. Acta* **2020**, *511*, 119814.

(28) Amini, M.; Haghdoost, M. M.; Bagherzadeh, M. Oxido-Peroxido Molybdenum(VI) Complexes in Catalytic and Stoichiometric Oxidations. *Coord. Chem. Rev.* **2013**, *257*, 1093–1121.

(29) Deubel, D. V.; Sundermeyer, J.; Frenking, G. Theoretical Studies of Molybdenum Peroxo Complexes $[MoO_n(O_2)_{3-n}(OPH_3)]$ as Catalysts for Olefin Epoxidation, *Inorg. Chem.* **2000**, *39*, 2314–2320.

(30) Ambroziak, K. New Dioxomolybdenum(VI) Complexes of Tetradentate Schiff Base as Catalysts for Epoxidation of Olefins. *J. Mol. Catal. Chem.* **2004**, *211*, 9–16.

(31) Mars, P.; van Krevelen, D. W. Oxidations Carried out by Means of Vanadium Oxide Catalysts. *Chem. Eng. Sci.* **1954**, *3*, 41–59.

(32) Doornkamp, C.; Ponec, V. The Universal Character of the Mars and Van Krevelen Mechanism. *J. Mol. Catal. Chem.* **2000**, *162*, 19–32.

(33) Khenkin, A. M.; Weiner, L.; Wang, Y.; Neumann, R. Electron and Oxygen Transfer in Polyoxometalate, $H_5PV_2Mo_{10}O_{40}$, Catalyzed Oxidation of Aromatic and Alkyl Aromatic

Compounds: Evidence for Aerobic Mars−van Krevelen-Type Reactions in the Liquid Homogeneous Phase. *J. Am. Chem. Soc.* **2001**, *123*, 8531–8542.

(34) Sheldon, R. A. A History of Oxygen Activation: 1773–1993. In *The Activation of Dioxygen and Homogeneous Catalytic Oxidation*; Barton, D. H. R., Martell, A. E., Sawyer, D. T., Eds.; Springer US: Boston, MA, 1993; pp 9–30.

(35) Sharpless, K. B.; Townsend, J. M.; Williams, D. R. Mechanism of Epoxidation of Olefins by Covalent Peroxides of Molybdenum(VI). *J. Am. Chem. Soc.* **1972**, *94*, 295–296.

(36) Yudanov, I. V.; Di Valentin, C.; Gisdakis, P.; Rösch, N. Olefin Epoxidation by Mono and Bisperoxo Complexes of Mo(VI): A Density Functional Model Study. *J. Mol. Catal. Chem.* **2000**, *158*, 189–197.

(37) Kühn, F. E.; Santos, A. M.; Abrantes, M. Mononuclear Organomolybdenum(VI) Dioxo Complexes: Synthesis, Reactivity, and Catalytic Applications. *Chem. Rev.* **2006**, *106*, 2455–2475.

(38) Grover, N.; Kuhn, F. E. Catalytic Olefin Epoxidation with (η^5-Cyclopentadienyl Molybdenum Complexes. *Curr. Org. Chem.* **2012**, *16*, 16–32.

(39) Campestrini, S.; Di Furia, F.; Rossi, P.; Torboli, A.; Valle, G. Comparison of the Relative Efficiency of Peroxomolybdenum Complexes as Oxidants of the Alcoholic Function. *J. Mol. Catal.* **1993**, *83*, 95–105.

(40) Veiros, L. F.; Gamelas, C. A.; Calhorda, M. J.; Romão, C. C. Chemoselective Sulfide and Sulfoxide Oxidations by $CpMo(CO)_3Cl$/HOOR: A DFT Mechanistic Study. *Organometallics* **2011**, *30*, 1454–1465.

(41) Arzoumanian, H.; Petrignani, J. F.; Pierrot, M.; Ridouane, F.; Sanchez, J. Preparation of an Oxoperoxocyanomolybdate(VI) Complex by Dioxygen Oxidation of an Oxocyanomolybdate(IV) Anion. Structure and Reactivity toward Phosphines and Olefins. *Inorg. Chem.* **1988**, *27*, 3377–3381.

(42) Lyashenko, G.; Saischek, G.; Judmaier, M. E.; Volpe, M.; Baumgartner, J.; Belaj, F.; Jancik, V.; Herbst-Irmer, R.; Mösch-Zanetti, N. C. Oxo-Molybdenum and Oxo-Tungsten Complexes of Schiff Bases Relevant to Molybdoenzymes. *Dalton Trans.* **2009**, *29*, 5655–5665.

(43) Nemykin, V. N.; Laskin, J.; Basu, P. Isolation, Characterization of an Intermediate in an Oxygen Atom-Transfer Reaction, and the Determination of the Bond Dissociation Energy. *J. Am. Chem. Soc.* **2004**, *126*, 8604–8605.

(44) Ueyama, N.; Yoshinaga, N.; Nakamura, A. Catalytic Air and Amine N-Oxide Oxidation of p-Substituted Benzoin by Molybdenum(VI) Complexes. Identification of the Deactivation Process by Dioxygen. *J. Chem. Soc. Dalton Trans.* **1990**, 387–394.

(45) Lyashenko, G.; Saischek, G.; Pal, A.; Herbst-Irmer, R.; Mösch-Zanetti, N. C. Molecular Oxygen Activation by a Molybdenum(IV) Monooxo Bis(β-Ketiminato) Complex. *Chem. Commun.* **2007**, 701–703.

(46) Matoga, D.; Szklarzewicz, J.; Samotus, A.; Lewiński, K. Crystal Structures of Mixed-Ligand Oxocyano Complexes of Molybdenum(IV) and Tungsten(IV) and Their Reactivity towards Molecular Oxygen Studied by IR Spectroscopy. *J. Chem. Soc. Dalton Trans.* **2002**, 3587–3592.

(47) Matoga, D.; Szklarzewicz, J.; Samotus, A.; Burgess, J.; Fawcett, J.; Russell, D. R. Preparation and Characterisation of $[M(CN)_4O(Pz)]^{2-}$ Complexes (M=Mo or W) and Their Reactivity towards Molecular Oxygen. *Polyhedron* **2000**, *19*, 1503–1509.

(48) Zwettler, N.; Grover, N.; Belaj, F.; Kirchner, K.; Mösch-Zanetti, N. C. Activation of Molecular Oxygen by a Molybdenum(IV) Imido Compound. *Inorg. Chem.* **2017**, *56*, 10147–10150.

(49) Zwettler, N.; Judmaier, M. E.; Strohmeier, L.; Belaj, F.; Mösch-Zanetti, N. C. Oxygen Activation and Catalytic Aerobic Oxidation by Mo(IV)/(VI) Complexes with Functionalized Iminophenolate Ligands. *J. Chem. Soc. Dalton Trans.* **2016**, *45*, 14549–14560.

(50) Bagherzadeh, M.; Haghdoost, M. M.; Amini, M.; Derakhshandeh, P. G. Molybdenum Oxo–Peroxo Complex: A Very Fast Catalyst for Oxidation and Reduction of Sulfur-Based Compounds. *Catal. Commun.* **2012**, *23*, 14–19.

(51) Fronczek, F. R.; Luck, R. L.; Wang, G. Synthesis, Characterization and Reactivity of $MoCl_2(O)(O_2)(OPR_3)_2$, OPR_3=$OPMePh_2$, $OPPh_3$; an Isomerization Catalyst for Some Allylic Alcohols. *Inorg. Chem. Commun.* **2002**, *5*, 384–387.

(52) Jimtaisong, A.; Luck, R. L. Synthesis and Catalytic Epoxidation Activity with TBHP and H_2O_2 of Dioxo-, Oxoperoxo-, and Oxodiperoxo Molybdenum(VI) and Tungsten(VI) Compounds Containing Monodentate or Bidentate Phosphine Oxide Ligands: Crystal Structures of $WCl_2(O)_2(OPMePh_2)_2$, $WCl_2(O)(O_2)(OPMePh_2)_2$, $MoCl_2(O)_2dppmO_2 \cdot C_4H_{10}O$, $WCl_2(O)_2dppmO_2$, $Mo(O)(O_2)_2dppmO_2$, and $W(O)(O_2)_2dppmO_2$. *Inorg. Chem.* **2006**, *45*, 10391–10402.

(53) Hammett, L. P. The Effect of Structure upon the Reactions of Organic Compounds. Benzene Derivatives. *J. Am. Chem. Soc.* **1937**, *59*, 96–103.

(54) Becke, A. D. A New Mixing of Hartree–Fock and Local Density Functional Theories. *J. Chem. Phys.* **1993**, *98*, 1372–1377.

(55) Perdew, J. P.; Ernzerhof, M.; Burke, K. Rationale for Mixing Exact Exchange with Density Functional Approximations. *J. Chem. Phys.* **1996**, *105*, 9982–9985.

(56) Zhao, Y.; Truhlar, D. G. The M06 Suite of Density Functionals for Main Group Thermochemistry, Thermochemical Kinetics, Noncovalent Interactions, Excited States, and Transition Elements: Two New Functionals and Systematic Testing of Four M06-Class Functionals and 12 Other Functionals. *Theor. Chem. Acc.* **2008**, *120*, 215–241.

(57) (a) Lee, S. C.; Holm, R. H. Toward an expanded oxygen atom transfer reactivity scale: Computational investigation of the energetics of oxo transfer reaction couples, *Inorg. Chim. Acta* **2008**, 361, 1166-1176. (b) Takatani, T.; Sears, J. S.; Sherrill, C. D. Assessing the Performance of Density Functional Theory for the Electronic Structure of Metal-Salens: The M06 Suite of Functionals and the d–Metals*, J. Phys. Chem. A* **2010**, *114*, 11714-11718. (c) Cerqueira, N. M. F. S. A.; Fernandes, P. A.; Gonzalez, P. J.; Moura, J. J. G.; Ramos, M.J. The sulfur shift: An activation mechanism for periplasmic nitrate reductase and formate Dehydrogenase, *Inorg. Chem*. **2013**, *52*, 10766-10772. (d) Lopatin, S. I.; Panin, A. I.; Shugurov, S. M.; Emelyanova, K. A. Gaseous titanium molybdates and tungstates: Thermodynamic properties and structures. *Rapid Comm. Mass Spect*. **2014**, *28*, 2636-2644. (e) Tilvez, E.; Cardenas-J. G. I.; Menendez, M. I.; Lopez, R. Understanding the Hydrolysis Mechanism of Ethyl Acetate Catalyzed by an Aqueous Molybdocene: A Computational Chemistry Investigation, *Inorg. Chem*. **2015**, *54*, 1223-1231. (f) Dhaked, D.K.; Bharatam, P. V. DFT study on the oxygen transfer mechanism in

nitroethenediamine based H-receptor antagonists using the bis-dithiolene complex as the model catalyst for *N*-oxide reductase enzyme, *J. Inorg. Biochem*. **2015**, *142*, 84-91.

(58) Arzoumanian, H. Molybdenum-Oxo and Peroxo Complexes in Oxygen Atom Transfer Processes with O_2 as the Primary Oxidant. *Curr. Inorg. Chem.* **2011**, *1*, 140–145.

(59) Yu, H.; Fu, Y.; Guo, Q.; Lin, Z. DFT Studies on Reactions of Transition Metal Complexes with O_2. *Organometallics* **2009**, *28*, 4443–4451.

(60) Arzoumanian, H.; Sanchez, J.; Strukul, G.; Zennaro, R. Dioxygen Ligand Transfer from Platinum to Molybdenum. Isolation of a Highly Reactive Molybdenum(VI) Oxoperoxo Dimer. In *The Activation of Dioxygen and Homogeneous Catalytic Oxidation*; Barton, D. H. R., Martell, A. E., Sawyer, D. T., Eds.; Springer US: Boston, MA, **1993**; pp 443–443.

(61) Harvey, J. N. Spin-Forbidden Reactions: Computational Insight into Mechanisms and Kinetics. *WIREs Comput. Mol. Sci.* **2014**, *4*, 1–14.

(62) Using the sobMECP program combined with the Gaussian program to search for the minimum energy intersection. http://sobereva.com/286

(63) González-Navarrete, P.; Sensato, F. R.; Andrés, J.; Longo, E. Oxygen Atom Transfer Reactions from Mimoun Complexes to Sulfides and Sulfoxides. A Bonding Evolution Theory Analysis. *J. Phys. Chem. A* **2014**, *118*, 6092–6103.

(64) Brown, S. N.; Mayer, J. M. Photochemical Generation of a Reactive Rhenium(III) Oxo Complex and Its Curious Mode of Cleavage of Dioxygen. *Inorg. Chem.* **1992**, *31*, 4091–4100.

(65) Akturk, E. S.; Yap, G. P. A.; Theopold, K. H. Dioxygen Activation by Non-Adiabatic Oxidative Addition to a Single Metal Center. *Angew. Chem. Int. Ed.* **2015**, *54*, 14974–14977.

(66) Herndon, J. W., III; Zink, J.; Lander, C.; Shao, Y.; Drayna, A. S.; Pacheco, A.; Richter-Addo, G.; Nicholas, K. M. Pathways for Dioxygen Evolution in the Thermal and Photochemical Conversion of (TTP)Mo(η^2-O_2)$_2$ to (TTP)MoO_2; manuscript in preparation, **2023**.

(67) Thornley, W. A.; Bitterwolf, T. E. Photochemistry of the Permanganate Ion in Low-Temperature Frozen Matrices. *Inorg. Chem.* **2015**, *54*, 3370–3375.

(68) Gubelmann, M. H.; Williams, A. F. The Structure and Reactivity of Dioxygen Complexes of the Transition Metals. In *Transition Metal Complexes Structures and Spectra*; Bacci, M.,

Fischer, J., Gubelmann, M. H., Koreň, B., Mathey, F., Melník, M., Nelson, J. H., Sivý, P., Valach, F., Williams, A. F., Eds.; Structure and Bonding; Springer: Berlin, Heidelberg, **1983**; pp 1–65.

(69) Swann, M. T.; Nicholas, K. M. Structural Effects on Dioxygen Evolution from Ru(V)−Oxo Complexes. *Eur. J. Inorg. Chem.* **2021**, *2021*, 3565–3577.

(70) Benassi, R.; Folli, U.; Sbardellati, S.; Taddei, F. Conformational Properties and Homolytic Bond Cleavage of Organic Peroxides. I. An Empirical Approach Based upon Molecular Mechanics and Ab Initio Calculations. *J. Comput. Chem.* **1993**, *14*, 379–391.

(71) Marenich, A. V.; Cramer, C. J.; Truhlar, D. G. Universal Solvation Model Based on Solute Electron Density and on a Continuum Model of the Solvent Defined by the Bulk Dielectric Constant and Atomic Surface Tensions. *J. Phys. Chem. B* **2009**, *113*, 6378–6396.

(72) R. A. Angnes, mechaSVG, GitHub repository, **2020**, doi: 10.5281/zenodo.3970267.

Graphical Abstract

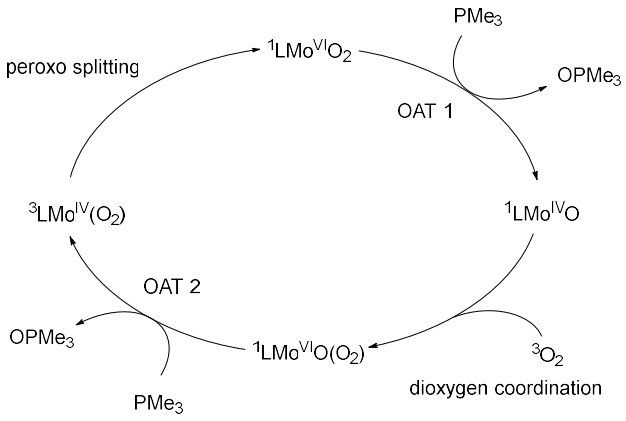

DFT and experimental study of the catalytic pathway for aerobic oxidation of phosphines by $LMoO_2$ (L=cy-salen) identifies four reaction stages: 1) *O*-atom transfer (OAT 1) to PMe_3 from the oxo-O of $LMoO_2$; 2) stepwise O_2 coordination to LMoO to form oxo-peroxo $LMo(O)(\eta^2\text{-}O_2)$; 3) novel OAT 2 from the oxo-group of the oxo-peroxo complex to PMe_3 gives monoperoxo $LMo(\eta^2\text{-}O_2)$; and 4) rare electronic isomerization (splitting) of the peroxo unit of $LMo(\eta^2\text{-}O_2)$ to regenerate $LMoO_2$.